

Effect of Hydraulic Fracturing Fluid Viscosity
on Stimulated Reservoir Volume for Shale Gas Recovery

BENNOUR Ziad

Acknowledgment

This study would not have been possible without the help and support of many people:

My deepest gratitude to my supervisor in *Kyoto University*; Professor *Tsuyoshi Ishida*, who was abundantly helpful and offered invaluable assistance, support and guidance all the time.

Also I wish to extend my gratitude to the reviewers of this manuscript, Professor *Weiren Lin* and Professor *Yoshitaka Nara* for their critical comments and suggestions that helped improving this study.

Gratitude is also a due to the co-supervisors: Professor *Sumihiko Murata*, Professor *Katsuaki Koike* and Professor *Youqing Chen* for their valuable support and advice.

Special thanks to my other colleagues in *Kyoto University*; Mr. *Yuya Nagaya*. Mr. *Shuhe Inue*, Mr. *Hiroto Yamashita*, Mr. *Yuto Tomonaga*, Mr. *Shouta Watanabe* and Mr. *Yuya Morishige* for their co-operation and valuable contributions to this research by providing help and assistance.

Thanks to the members of *3D-Geoscience Inc.*; Dr. *Yoshiki Nakayama* and Dr. *Qu Chen* for their support through providing facilities, knowledge, technical help and advices throughout this research.

Thanks also to the management and members of *JOGMEC*, especially; Ms. *Yu Nagano* and Mr. *Takashi Akai* for their valuable contribution, advice and the continuous support.

Finally; Thanks to the personnel at *Kushiro Coal Mine Co. Ltd.*, for their valuable assistance by providing rock blocks that were used to make cores for the experiments in this study.

Ziad Bennour
Kyoto University, Graduate School of Engineering
Department of Civil and Earth Resources Engineering
January, 2017

Table of Contents

Front matters	i
Acknowledgement	ii
Table of Contents	iii
Chapter 1 – Introduction	1
1.1 Background	1
1.2 Literature Review	2
1.3 The Study Objective	5
1.4 References	6
Chapter 2 – Features of CO₂ Fracturing Deduced from Acoustic Emissions	11
2.1 Background	11
2.2 Methods	12
2.2.1 Specimens and Experimental Setup	12
2.2.2 Method of Fluid Injection	15
2.2.3 Methods for Monitoring AE, Pressure, and Temperature	18
2.2.4 Observation of Fractures with Fluorescent Resin	19
2.3 Results	19
2.3.1 Changes in Fluid Pressure and AE Count Rate	20
2.3.2 AE Source Locations	22
2.3.3 Induced Fracture Patterns Observed with the Fluorescent Method	25
2.4 Effect of Fluid Viscosity	29
2.4.1 Breakdown Pressure and Apparent Tensile Strength	30
2.4.2 AE Distribution	33
2.4.3 Fracturing Mechanism Deduced from P Wave Polarity of AE	34
2.4.4 Fracture Features Deduced from Microscopic Observation	35
2.5 Discussion	36
2.6 Conclusions	38
2.6 References	40
Chapter 3 – Fracturing Mechanism in Hydraulic Fracturing of Shale Cores	46
3.1 Background	46
3.2 Methods	47
3.2.1 Cores and Experimental Setup	47
3.2.2 Method of Fluid Injection	49
3.2.3 Methods for Monitoring AE, Pressure, and Temperature	49

3.2.4 Observation of Fractures with Fluorescent Resin	50
3.3 Results	50
3.3.1 Testing Observations under Ambient Conditions	51
3.3.2 Testing Observations under Uni-axial loading	54
3.3.3 Analysis and Determination of Mode of Fracturing	56
3.3.4 Microscopic examination of fractures	57
3.4 Discussion	59
3.5 Conclusions	62
References	63
Chapter 4 – Stimulated Reservoir Volume Using the Fluorescence Method.....	65
4.1 Background	65
4.2 Methods	66
4.2.1 Rock Samples and HF Experiments.....	66
4.2.2 Preparation of Samples for Microscopy Observation	67
4.2.3 Image Processing and Evaluation Technique	68
4.3 Results and Discussion	70
4.4 Conclusions	74
References	75
Chapter 5 – Conclusions	79

Chapter 1

Introduction

1.1 Background

Energy shortage is one of the world's concerns because of the high demand to use resources for power purposes by the industrial societies. As the demand rises, these natural resources are diminishing, because simply they are in limited supply. Many global initiatives try to resolve the energy shortage and also increase the regulations and restriction on carbon dioxide (CO₂) emissions. Combined strategies are set to solve the energy problem by maximizing energy efficiency, optimizing energy use and developing new sources of clean energy such as shale gas.

Shale gas refers to the natural gas trapped within formations of shale, a fine-grained sedimentary rock that can be a rich source of petroleum and natural gas. However, the low permeability of shale greatly inhibits the flow of gas from reservoir rocks to production wells. The economic viability of producing natural gas from shale formations depends highly on the effective stimulation of reservoirs, which is mainly achieved by combining the horizontal or directional drilling with planned multistage hydraulic fracturing (HF). Multistage HF stimulation on wells is a constant routine for the recovery of oil and gas from low permeability sedimentary reservoirs in shale gas provinces in the North America (e.g. King, 2010). This practice has been in use for long time and proved successful especially in shale gas reservoirs (Arthur et al., 2008).

According to Economides (2010), 90% of the natural gas wells in North America are being hydraulically fractured. In the past decade, the total number of HF jobs across the world is about 2.5 million which is a 300% increase compared to the past decade. The estimated size of the fracturing market is as high as 13 billion dollars in North America alone. So it becomes important to understand the fracturing process through field scale experiments and controlled laboratory experiments.

Shale gas exploration is starting in many other countries with sediments being potential future targets. Therefore constraining the probability of making unusually tall

hydraulic fractures in sedimentary rocks is critically important, as it will help avoid the unintentional penetration of shallower rock formation that might be important aquifers or subsurface geological storage sites (Davis et al. 2012).

Monitoring of acoustic emissions (AE) induced by HF provides remote mapping of the fracture geometry, azimuth, connectivity, density and length. When performed in real-time, this allows changes to be made to the fracturing program in real-time, including modifications to pump pressure and rate or proppant mesh; operators can also identify the fluid movement patterns and fracture containment (Chitrala et al., 2013). Dynamic feedback provides a mechanism to improve and optimize the stimulation. The concern is the accuracy of the hypocenter locations and their interpreted stimulated reservoir volumes (SRV) (Chitrala et al., 2013).

1.2 Literature Review

Stimulation by HF as a technique for improved hydrocarbon production from low permeability reservoirs dates back to the late 1940s (Montgomery and Smith, 2010). The HF is the process of initiation and propagation of fractures by injection of a fluid at a pressure higher than the strength of the rock. The technique of stress measurements using HF was developed by Hubbert and Willis (1957). Building on this work, Cleary (1958) presented an early version of HF theory and the possibility of fracture control. Since then, many theoretical and experimental investigations have been conducted (e.g. Zoback et al., 1977; Schmitt and Zoback, 1989; Haimson and Cornet, 2003).

Due to the complexity of unconventional reservoirs, it is challenging to predict the initiation and propagation of hydraulic fractures (Hagstrom and Adams 2012). That is because the underground formations are subjected to complex stress fields and affected by various geological processes, as described by Amadei and Stephansson (1977), also by Zang and Stephansson (2010).

The complex in-situ stress state and distribution of rocks of varied attributes, which may change the profile of fractures induced by HF (Gu et al., 2008); the existence of arbitrary pre-existing interfaces may diversify or arrest HF (Zhang et al., 2010); the temperature effect (Ribeiro and Horne, 2013); the fluid loss and transport of proppant; the

competition between fractures, and its recession and closure (Adachi et al., 2007). The stress condition is important in HF because they control the magnitude of pressure required to create and propagate a fracture, the direction of the fracture and the fracture shape under homogeneous, isotropic and elastic rock mass. However, in actual rock mass, the fracture extending direction by HF is also a function of several variables, including anisotropy of rock strength. Sun et al. (2011) investigated fracture extension during HF in oil shale and found that the fractures are elliptical and that fractures extend along different directions due to anisotropic properties.

In shale gas exploitation, measurements of the AE caused by HF (e.g. Maxwell et al., 2002) have shown that fractures can extend for several hundred meters upwards and downwards from the wellbore (Fisher and Warpinski, 2011). As the goal of HF is to create high conductivity fracturing networks as flow paths for gas, it is necessary for HF to activate and connect existing natural fractures to generate a large fractures network (Clarkson et al., 2012; 2013). The success or failure of HF often depends on the resulted SRV which is characterized by the quantity and the quality of the HF induced fractures network (Mayerhofer et al., 2010). However, the induced HF networks are difficult to be observed in the field. Even in lab experiments, only a 2-D section of the fractures network is examined and only few attempts have been made to achieve real characterization of the laboratory HF geometry (Kear et al., 2013).

Laboratory studies of HF vary from small-scale rock samples with several cubic centimeters to large ones with one cubic meter or more (Haimson, 1981). Since it is easy to control the stress conditions and make artificial structures within samples, HF process with different stress field and rock structures can be conveniently studied. Especially in large scale experiments, it is possible to build a full size borehole, or to control the development of hydraulic fractures (Bai et al., 2006), and the HF geometries can be easily obtained and parametric study on such experiments can be quite handy.

Ishida et al. (2004; 2012; 2013) have previously conducted HF experiments using viscous oil, water and CO₂, and found that low viscosity fluids such as CO₂ tend to induce widely extending fractures with many branches. These fractures should be better

suitable for producing shale gas because they have a larger surface area within the shale than those induced by water.

In shale gas industry, it is necessary to develop new reservoir fracturing and enhanced gas recovery technologies to reduce water usage to guarantee the environmental sustainability and boost individual well production (Peng et al. 2015). The CO₂ is often used for miscible flooding in depleted petroleum reservoirs to react with residual oil to change its properties, allowing it to flow more freely and enhances oil recovery (Melzer, 2012). The uses of low viscosity HF fluids such as CO₂ for well stimulation have been considered because it eliminates formation damage and also reduce the residual fracturing fluid (Sinal and Lancaster, 1987; Liao et al., 2009).

Besides, the CO₂ also has higher affinity for shale than methane (CH₄) does; CO₂ absorption should be preferred over CH₄ absorption with a molecular ratio of up to 5:1 (Nuttall et al., 2006; Nuttall, 2010). The dependence of the affinity on total organic carbon (Weniger et al., 2010), pore structure (Ross and Bustin, 2009), moisture content (Yuan et al., 2014), and pressure and temperature (Khosrokhavar et al., 2014) have been investigated and examined in laboratory experiments.

Numerical simulation suggests that CO₂ injection can increase gas production by 7% in Marcellus shale (Godec et al., 2013). They also suggest that storage with enhanced CH₄ gas recovery is feasible in the *New Albany* shale (Liu et al., 2013) and *Haynesville* shale (Middleton et al., 2015). These studies have led to the acceptance of the possibility of CO₂ storage in shale formations (NETL, 2012).

The underground sequestration of CO₂ is a promising and feasible method to mitigate the greenhouse gas effect by decreasing the amount of CO₂ emitted to the atmosphere. The method is not economically viable due to the high costs of the capture, transportation, and underground injection of CO₂. If this method can offer economic benefits to compensate for its costs, it will be much more eagerly developed and adopted.

1.3 The Study Objective

This research focuses on features of HF and how it can be quantified in the laboratory. In addition, this study focuses on the effect of HF fluid viscosity on fracturing mechanism and the resulting SRV.

In this regard, HF experiments were conducted in cubic specimens of granite under tri-axial stresses, using viscous oil, water, liquid carbon dioxide (L-CO₂) and super critical state carbon dioxide (SC-CO₂). Also, another set of HF experiments were conducted in cylindrical cores of shale under uni-axial stresses, using three types of fracturing fluid: viscous oil, water, and L-CO₂.

In the experiments, AE was monitored to investigate the effect of the viscosity of various HF fluids on induced fracture features and on fracturing mechanism. Since the granite cubes have rift plane and the shale cores have sedimentary plane, the effects of anisotropy due to these inherent weak planes on the fracture growth were investigated under the applied stress condition. In addition, this study investigates the micro-fractures network resulted in laboratory HF experiments in 2-D section by using a fluorescent method (Nishiyama and Kusuda, 1994) that can provide the advantage tracing HF fractures in a thin polished section. Supported by advanced computerized image analysis, which is useful to visualize and evaluate fractures network, SRV induced created by HF has been evaluated.

The results of this research would contribute to not only shale gas production but also projects of enhanced geothermal systems (EGS), CO₂ capture and storage (CCS).

References

Adachi J., Siebrits E., Peirce A. and Desroches J. (2007). Computer Simulation of Hydraulic Fractures. *International Journal of Rock Mechanics and Mining Sciences*, 44 (5), p. 739-757.

Amadei B. and Stephansson O. (1977). *Rock Stress and its Measurement*. Chapman & Hall.

Arthur J. D., Bohm B. and Layne M. (2008). Hydraulic Fracturing Considerations for Natural Gas Wells of the Marcellus Shale. *Proceedings of the Ground Water Protection Council Annual Forum*, 1-16. Ohio, USA.

Bai M., Green S., Casas L. and Miskimins J. (2006). 3-D Simulation of Large Scale Laboratory Hydraulic Fracturing Tests. *ARMA the 41st U.S. Symposium on Rock Mechanics*. Golden, Colorado, USA.

Chitrala Y., Moreno C., Sondergeld C. and Rai C. (2013). An Experimental Investigation into Hydraulic Fracture Propagation under Different Applied Stresses in Tight Sands Using Acoustic Emissions. *Journal of Petroleum Science and Engineering* 108, p. 151–161.

Clarkson C., Nobakht M., Kaviani D. and Ertekin T. (2012). Production Analysis of Tight-gas and Shale-gas Reservoirs Using the Dynamic Slippage Concept. *SPE Journal*, 17/1, p. 230-242. SPE-144317-PA.

Clarkson C., Solano N., Bustin R., Bustin A., Chalmers G., He L., Melnichenko Y., Radlinski A. and Blach T. (2013). Pore Structure Characterization of North American Shale Gas Reservoirs Using USANS/SANS, gas adsorption, and mercury intrusion. *Journal of Fuel*, 103, p. 606-613.

Cleary J. (1958). *Hydraulic Fracture Theory Part II - Fracture Orientation and Possibility of Fracture Control*. Division of the Illinois state geological survey, Circular 252.

Davies R., Mathias S., Moss J., Hustoft S. and Newport L. (2012) Hydraulic Fractures: How far can they go?. *Marine and Petroleum Geology*, 37(1), p. 1-6, ISSN 0264-8172.

- Economides M. (2010). International State of Hydraulic Fracturing. .
(<http://queensland.spe.org/images/Queensland/articles/54/International%20State%20of%20Hydraulic%20Fracturing.pdf>).
- Fisher K. and Warpinski N. (2011). Hydraulic Fracture-Height Growth: Real Data. *Journal of Society of Petroleum Engineers*, 27, P. 8-19.
- Godec M., Koperna G., Petrusak R. and Oudinot A. (2013). Potential for Enhanced Gas Recovery and CO₂ Storage in the Marcellus Shale in the Eastern United States. *International Journal of Coal Geology*, 118, p.95-104.
- Gu H., Siebrits E. and Sabourov A. (2008). Hydraulic-Fracture Modeling with Bedding Plane Interfacial Slip, in: SPE Eastern Regional/AAPG Eastern Section Joint Meeting, Society of Petroleum Engineers, Pittsburgh, Pennsylvania, USA,
- Hagstrom E. and Adams J. (2012) Hydraulic Fracturing: Identifying and Managing the Risks. *Environmental Claims Journal* , 24 (2), p. 93-115.
- Haimson B. (1981). Large Scale Laboratory Testing of Hydraulic Fracturing. *Geophysical Research Letters*, 8 (7), p. 715-718.
- Haimson B. and Cornet F. (2003). ISRM Suggested Methods for Rock Stress Estimation—Part 3: Hydraulic Fracturing (HF) and/or Hydraulic Testing of Pre-Existing Fractures (HTPF). *International Journal of Rock Mechanics and Mining Sciences*, 40, p.1011-1020.
- Hubbert M. and Willis D. (1957). Mechanics of Hydraulic Fracturing. *Petroleum transactions AIME*, 210, p.153-168.
- Ishida T., Chen Q., Mizuta Y. and Roegiers J. (2004). Influence of Fluid Viscosity on the Hydraulic Fracturing Mechanism. *Transactions of the ASME, Journal of Energy Resource Technology*, 126, p.190-200.
- Ishida T., Aoyagi K., Niwa T., Chen Y., Murata S., Chen Q. and Nakayama Y. (2012). Acoustic Emission Monitoring of Hydraulic Fracturing Laboratory Experiment with

Supercritical and Liquid CO₂. *Geophysical Research Letters*, 39, L16309, doi: 10.1029/2012GL052788.

Ishida T., Nagaya Y., Inui S., Aoyagi K., Nara Y., Chen Y., Chen Q. and Nakayama Y. (2013). AE monitoring of Hydraulic Fracturing Experiments with CO₂ and Water. *Proceedings of Eurock, Wroclaw, Poland*, p. 957-962.

Kear J., White J., Bungler A., Jeffrey R. and Hessami M. (2013). Three Dimensional Forms of Closely-Spaced Hydraulic Fracture. *Effective and Sustainable Hydraulic Fracturing*, Chapter 34, ISBN 978-953-51-1137-5.

Khosrokhavar R., Wolf K. and Bruining H. (2014). Sorption of CH₄ and CO₂ on a Carboniferous Shale from Belgium using a Manometric setup. *International Journal of Coal Geology*, 128/129, p.153-161.

King G. (2010). Thirty Years of Shale Gas Fracturing: What Have We Learned?. *Society of Petroleum Engineers*, 28, p. 323-344.

Liao S., Brunner F. and Mattar L. (2009). Impact of Ignoring CO₂ Injection Volumes on Post-Frac PTA. *Proceedings of Canadian International Petroleum Conference*. Calgary, Alberta, Canada.

Liu F., Ellett K., Xiao Y. and Rupp J. (2013). Assessing the Feasibility of CO₂ Storage in the New Albany Shale (Devonian- Mississippian) with Potential Enhanced Gas Recovery Using Reservoir Simulation. *International Journal of Greenhouse Gas Control*, 17, p.111-126.

Maxwell S., Urbancic T., Steinsberger N. and Zinno R. (2002). Micro seismic Imaging of Hydraulic Fracture Complexity in the Barnett Shale. *Society of Petroleum Engineers, Proceedings of SPE Annual Technical Conference*, 29 September-2 October, 2002, San Antonio. USA

Mayerhofer M., Lolon E., Warpinski N., Cipolla C., Walser D. and Rightmire C. (2010). What Is Stimulated Reservoir Volume?. *Society of Petroleum Engineers, SPE* 25 (1): doi:10.2118/119890-PA.

Melzer L. (2012). Carbon Dioxide Enhanced Oil Recovery (CO₂-EOR): Factors Involved in Adding Carbon Capture, Utilization and Storage (CCUS) to Enhanced Oil Recovery. Proceedings of the Annual CO₂ Flooding Conference, February, 2012. Midland, Texas, USA.

Middleton R., Carey J., Currier R., Hyman J., Kang Q., Karra S., Jiménez-Martínez J., Porter M. and Viswanathan H. (2015). Shale Gas and Non-Aqueous Fracturing Fluids: Opportunities and Challenges for Supercritical CO₂. *Journal of Applied Energy*, 147, p.500-509.

Montgomery C. and Smith M. (2010). Hydraulic Fracturing: History of an Enduring Technology. *Journal of Petroleum Technology*, 62, p. 26-32.

NETL (2012). Carbon Sequestration Atlas of the United States and Canada. 4th edition. National Energy Technology Laboratory, U.S. Department of Energy, [http://www.netl.doe.gov/technologies/carbon seq/refshelf/atlasIV/Atlas-IV-2012.pdf](http://www.netl.doe.gov/technologies/carbon_seq/refshelf/atlasIV/Atlas-IV-2012.pdf)

Nishiyama T., and Kusuda H. (1994). Identification of Pore Spaces and Micro Cracks Using Fluorescent Resins. *International Journal of Rock Mechanics and Mining Science & Geomechanics Abstracts*, 31, p. 369–375.

Nuttall B., Drahovzal J., Eble C. and Bustin R. (2006). CO₂ Sequestration in Gas Shales of Kentucky. Proceedings of the 5th Annual Conference on Carbon Capture and Sequestration, Poster No. 106. Alexandria, Virginia, USA.

Nuttall B. (2010). Reassessment of CO₂ Sequestration Capacity and Enhanced Gas Recovery Potential of Middle and Upper Devonian Black Shales in the Appalachian Basin. In: MRCSP Phase II Topical Report, Oct. 2005 - Oct. 2010. Kentucky Geological Survey. Lexington, Kentucky, USA.

Peng P., Ling K., He J. and Liu Z. (2015). Shale Gas Reservoir Treatment by a CO₂ Based Technology. Proceedings of 2nd Biennial CO₂ for EOR as CCUS Conference. October 4 - 6, Houston, Texas, USA.

Ribeiro P. and Horne R. (2013). Pressure and Temperature Transient analysis: Hydraulic Fractured Well Application, SPE Annual Technical Conference and Exhibition, Society of Petroleum Engineers, New Orleans, Louisiana, USA.

Ross D., and Bustin R. (2009). The Importance of Shale Composition and Pore Structure upon Gas Storage Potential of Shale Gas Reservoirs. *Journal of Marine and Petroleum Geology*, 26, p.916–927.

Schmitt D. and Zoback M. (1989). Poro-Elastic Effects in the Determination of the Maximum Horizontal Principal Stress in Hydraulic Fracturing Tests; A Proposed Breakdown Equation Employing a Modified Effective Stress Relation for Tensile Failure. *International Journal of Rock Mechanics and Mining Sciences & Geomechanics Abstracts*, 26:p.499-506.

Sinal M. and Lancaster G. (1987). Liquid CO₂ Fracturing: Advantages and Limitations. *Journal of Canadian petroleum technology*, 26(5), p. 26–30.

Sun K., Tan J. and Wu D. (2011). The Research on Dynamic Rules of Crack Extension During Hydraulic Fracturing for Oil Shale In-Situ Exploitation. *Proceedings of International Conference on Environmental Science and Engineering (ICESE 2011)*. *Procedia Environmental Sciences*, 12 (2012), p.736-743.

Zang A. and Stephansson O. (2010) *Stress Field of the Earth's Crust*. ISBN 978-1-4020-8444-7.

Zhang G., Liu H., Zhang J., Wu H. and Wang X. (2010). Three-Dimensional Finite Element Simulation and Parametric Study for Horizontal Well Hydraulic Fracture. *Journal of Petroleum Sciences and Engineering*, 72(34), p. 310-317.

Chapter 2

Features of CO₂ Fracturing Deduced from Acoustic Emissions

2.1 Background

The underground sequestration of carbon dioxide (CO₂) is a promising and feasible method to mitigate the greenhouse gas effect by decreasing the amount of CO₂ emitted to the atmosphere. The method is not economically viable, however, due to the costs for the capture, transportation, and underground injection of CO₂. If this method can offer economic benefits to compensate for its costs, it will be much more eagerly developed and adopted.

CO₂ is often used for miscible flooding to enhance oil recovery in depleted petroleum reservoirs, and the use of CO₂ as a fracturing fluid for well stimulation has been considered because it eliminates formation damage and residual fracturing fluid (Sinal and Lancaster, 1987; Liao et al., 2009). In addition, CO₂ has higher affinity for shale than methane (CH₄) does (Nuttall et al., 2006), and it is suggested that CO₂ is preferentially absorbed over CH₄ with a molecular ratio of up to 5:1 by molecule (Nuttall et al., 2010). The dependences of the affinity on total organic carbon (Weniger et al., 2010), pore structure (Ross and Marc Bustin, 2009), moisture content (Yuan et al. 2014) and pressure and temperature (Khosrokhavar et al. 2014) are examined through laboratory experiments. The numerical simulations using this knowledge suggested that CO₂ storage to enhance CH₄ gas recovery is feasible in the *New Albany* shale (Lui et al., 2013) and *Haynesville* shale (Middleton et al. 2015).

Furthermore in the Marcellus shale, CO₂ injection can realize 7% enhanced gas production (Godec et al., 2013). Through these efforts, it has been accepted as one option to store CO₂ in shale formations (NETL, 2012). On the other hand, for geothermal energy extraction from hot dry rock, CO₂ is considered for use as fracturing and circulating fluid because it reduces the power requirements for circulating pumps and eliminates scale formation in surface piping by its inability to dissolve mineral species (Brown, 2000). Following the concept, Pruess (2006) compared CO₂ with water in the thermo-physical

properties, the flow behavior and chemical aspects, and he concluded that CO₂ is superior to water as working fluid of an enhanced geothermal system.

Usually, CO₂ is injected into rocks at a depth of more than 1,000 m for underground sequestration and enhanced oil recovery and sometimes more than 3,000 m for shale gas exploitation and enhanced geothermal system development. The temperature and pressure at such great depth usually form supercritical CO₂ (SC-CO₂), but the lower temperatures present in special geological conditions can induce a liquid state. The viscosity of liquid CO₂ (L-CO₂) is one order lower than that of normal liquid water, and the viscosity of SC-CO₂ is much lower still. Features of fractures induced by hydraulic fracturing (HF) using such a low viscosity fluid are expected to be different from those by conventional HF using water. Differences of the fractures features induced by CO₂ are only observed in laboratory with un-aided eyes by Kizaki et al. (2013) and examined through numerical simulations by Zhou and Burbey (2014).

Ishida et al. (2012) have already made a preliminary experiment to monitor acoustic emission (AE) induced by HF experiments only using SC-CO₂ and L-CO₂ in granite specimens under hydrostatic loading. After the experiment, the injection of SC-CO₂, L-CO₂, water and viscous oil was extended under a tri-axial deviatoric stress condition.

This chapter discusses differences among the four fluids, focusing on breakdown pressure, induced fractures characterized by the distribution of located AE sources and the fracturing mechanism derived from statistics of polarities in P wave initial motions of AE events. In addition, the fractures induced by the injection were observed microscopically using the fluorescent method (Nishiyama and Kusuda, 1994 and Chen et al. 2015).

2.2 Methods

2.2.1 Specimens and Experimental Setup

Eight cubes (170×170×170 mm) of granite with a 20 mm diameter central hole were used. The granite is produced in *Kurokami-jima* Island in *Seto* Inland Sea in

Southwestern *Japan*. The material is commonly known as *Kurokami-jima* granite. The modal composition of the samples for these experiments was about 40 % potassium feldspar, 36 % plagioclase, 21% quartz, and 3% micas and accessories. The mean grain size was about 2 mm, and some coarse potassium feldspar grains whose size more than 5 mm were observed.

To confirm the reproducibility of the experimental results, two specimens were used for each of the fracturing fluids: SC-CO₂, L-CO₂, and viscous oil, water, (Table 2.1). The inherent rift plane of the granite specimen was oriented to correspond to the YZ plane in the Cartesian coordinate system (Figure 2.1).

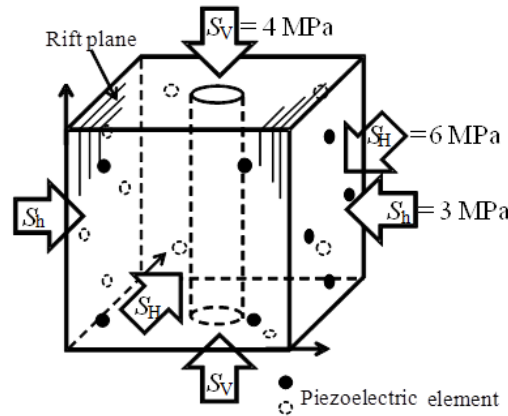


Figure 2.1 Coordinate system and loading condition of the specimen. The filled circles indicate the piezoelectric elements used as AE sensors at open positions, while the open circles with broken lines indicate those at hidden positions behind the specimen (after Ishida et al., 2012).

As shown in Table 2.1, the average P wave velocities measured along the Y and Z directions were around 5.0 km/s, whereas that along the X direction normal to the rift plane was around 4.5 km/s. The P wave velocities were measured before the experiments without any confining pressure.

Results of Brazilian tests with the discs oriented to make fracture along the rift plane on 33 cylindrical samples of the same kind of *Kurokami-jima* granite, measuring 45 mm in diameter and 30 mm in length, showed an average tensile strength of 3.38 MPa with a standard deviation of 0.21 MPa (Ishida et al., 2005).

Table 2.1 Specimen number, fracturing fluid, and P wave velocity.

Specimen no.	Fracturing fluid	P wave velocity (km/s)		
		V_x	V_y	V_z
G1115	SC-CO ₂	4.25	4.86	4.72
G1202	SC-CO ₂	5.16	5.68	5.67
G1213	L-CO ₂	4.88	5.32	5.26
G1209	L-CO ₂	4.75	5.40	5.33
G1102	Water	4.05	4.86	4.72
G1103	Water	4.25	5.00	4.72
G1114	Oil	4.05	4.72	4.60
G1112	Oil	4.25	4.86	4.60
Average		4.46	5.09	4.95

Effective porosity of the granite was 0.84 %, where the pore and the bulk volumes were measured with the saturation and the buoyancy methods, respectively (International Society for Rock Mechanics, 1979) and its intrinsic permeability obtained by air permeability test for hollow cylinder samples was around $9 \times 10^{-19} \text{ m}^2$ (Ishida et al., 2006). The intrinsic permeability corresponds to $1 \times 10^{-11} \text{ m/s}$ of hydraulic conductivity, which is within the extent from 10^{-12} to 10^{-8} m/s for general granitic rock shown by Vutukuri and Katsuyama (1994).

To monitor AE events induced by the fluid injection, four cylindrical PZT elements 4 mm in diameter and 4 mm thick were glued on each of the four lateral surfaces (total of 16 elements) of the specimen (Figure 2.1). To apply confining pressures, each lateral surface was covered with a 6 mm thick hard nylon sheet with four 5 mm diameter holes in the positions of the PZT elements. The PZT element wires were guided through grooves in the surface of the sheet, and the sheet was covered again with another 4 mm thick hard nylon sheet.

The specimen was placed in dry condition in a cylindrical pressure cell, except only the case of SC-CO₂ injection where the cell was filled with hot water to prevent the injected CO₂ from cooling. Four bow-shaped spacer blocks were inserted between the specimen and the inner wall of the pressure cell, and placed a flat jack between the specimen and each spacer block to apply pressure in the X and Y directions (Figure 2.2).

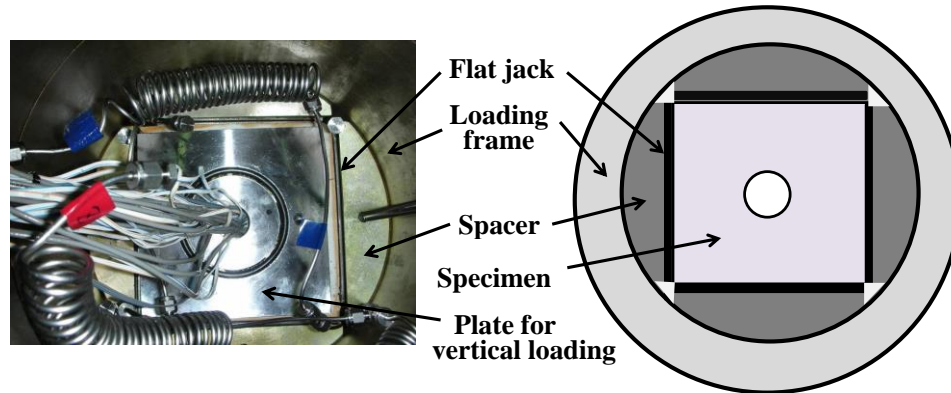


Figure 2.2 Photo (left) and cross-sectional schematic (right) of a specimen, flat jacks, and spacers set in the loading frame. In the photo, the specimen is set under the plate for the vertical loading (after Ishida et al., 2016).

In the Z direction, flat jacks were placed between the specimen and loading plates supported by the end caps on the top and bottom of the pressure cell. In all experiments, confining pressures of 3, 6, and 4 MPa were applied in the X , Y , and Z directions, respectively, to provide the deviatoric stress. The stress magnitudes of 3 and 6 MPa were selected following the solution by Kirsch (1898) so as to keep compressive stress larger than 3 MPa in the tangential direction all along the hole wall. The minimum tangential stress of 3 MPa induced at the points of the Y direction along the hole wall did not exceed the capacity of the injection pump and pipe line to induce HF, and the maximum stress of 15 MPa induced at those of the X direction was sufficiently smaller than that inducing the borehole breakout.

The stress magnitude of 4 MPa in the Z direction was selected so as to be between 3 and 6 MPa in the X and Y directions. Although the confining pressures increases the P wave velocities, these increases were ignored in calculation of AE source location, because they were expected to only vary around 0.1 to 0.3 km/s in the measurements of granite under confining pressure from 0 to 200 MPa (Sano et al., 1992).

2.2.2 Method of Fluid Injection

Figure 2.3 shows the packer inserted into the central hole of the samples to inject the fracturing fluids, including CO_2 . The packer had a 60 mm pressurizing section sealed with two O-rings at each end. The pressurizing section was centered along the hole. In all

of the experiments, the fracturing fluid was injected under the control of syringe pump to keep the same constant flow rate of 10 mL/min, and stopped the injection just after HF was induced, which was indicated by a sudden pressure drop.

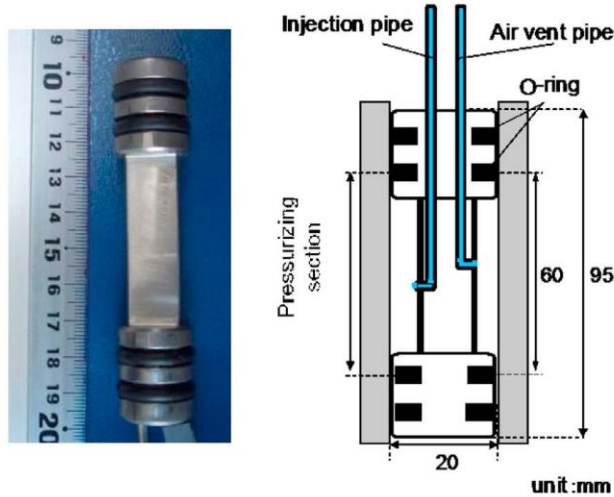


Figure 2.3 Straddle packer used to inject fracturing fluid including CO₂. Photo (left) and a cross-sectional schematic illustration (right) of the packer (after Ishida et al., 2012).

Figure 2.4 shows the injection system used for the HF experiments. To make SC-CO₂, the CO₂ was fed from a bomb to a syringe pump cylinder, which had a capacity of 266 mL. To fill the cylinder as much as possible, the CO₂ was cooled to keep it in the liquid state by circulating coolant in a cooling unit above the cylinder.

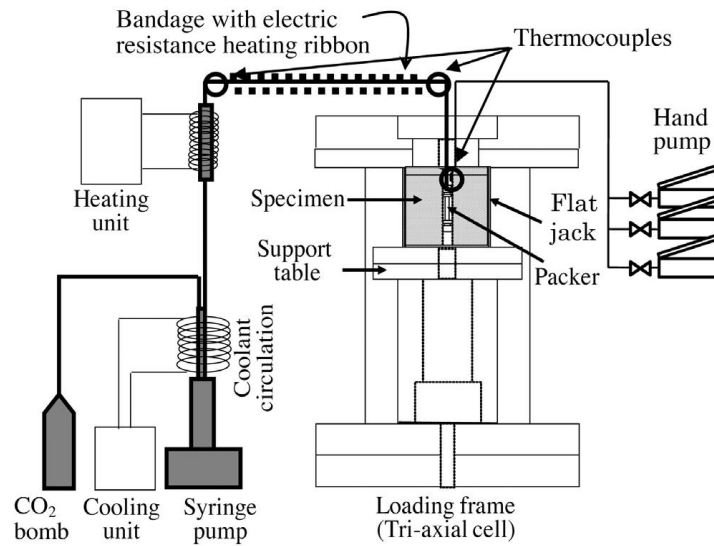


Figure 2.4 Schematic of system for injecting fracturing fluid and loading confining pressure (after Ishida et al., 2012).

The phase diagram in Figure 2.5 shows that CO₂ becomes supercritical when the temperature is higher than 31.0 °C and the pressure is greater than 7.38 MPa.

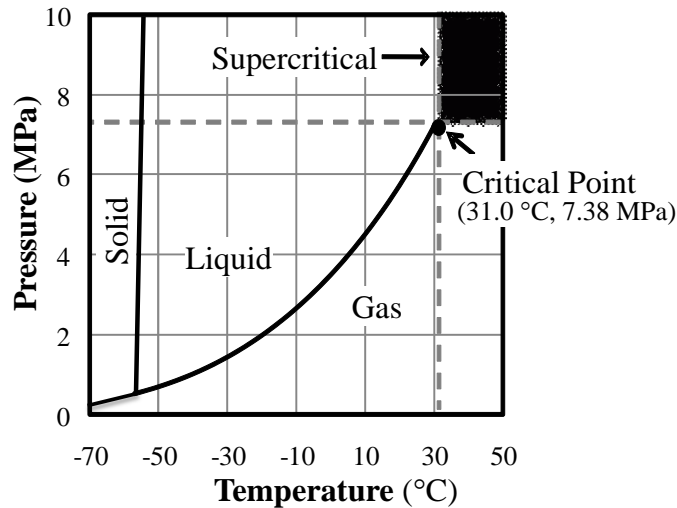


Figure 2.5 Phase diagram of CO₂.

After discharging L-CO₂ from the cylinder of the syringe pump at a constant flow rate of 10 mL/min, it was heated with a heater unit. The temperature was maintained at 55 °C by bandaging electric resistance heating ribbon along the pipe connecting the heater unit to the packer (Figure 2.4). In addition, the cell containing the specimen was filled with hot water at a temperature of around 45 °C to prevent the injected CO₂ from cooling.

Although the thermal properties of the *Kurokami-jima* granite were not measured, because the temperature in the specimen did not easily increase within 1 hour or so for the SC-CO₂ experiment, even when the outside of the specimen was warmed with the hot water and the wall of the injection hole wall with SC-CO₂. This expectation comes from the experiences in the heater test in a block of *Inada* granite whose thermal conductivity is 3.3 W/(m·K), specific heat is 0.72 J/(g·K) (Ishida et al., 1990) and density is 2.6×10³ kg/m³ (Lin, 2002). The similar tendency was also found in heater test in a block of *Lac du Bonnet* granite by Jansen et al. (1993). Thus, during the experiment, it is most likely that the temperature of the specimen only in the vicinity of the surfaces and the hole wall was kept around 40 °C, while the temperature in the specimen was kept at the room temperature around 20 °C in which the specimen was left more than one week before the

experiments. Although the specimen was soaked in hot water for around 1 hour, the water was not expected to infiltrate around the injection hole owing to the specimen's low permeability, and the HF was induced under almost dry conditions based on experiences from similar previous experiments.

For the other fluids, including L-CO₂, HF was also induced under dry conditions at room temperature, because the fluids were fed to the packer without heating or filling the cell with water.

2.2.3 Methods for Monitoring AE, Pressure, and Temperature

The PZT elements glued onto the specimen had a resonance frequency of 300 kHz and they were covered with an aluminum sheet to avoid electromagnetically induced noise. They were also covered with heat shrinkable tubes and silicone rubber to provide a waterproof barrier for SC-CO₂ fracturing.

The AE signals were amplified by 72 to 84 dB in total (36 dB in a pre-amplifier and 36 to 48 dB in a signal conditioner), processed with a band-pass filter between 80 kHz and 1 MHz, and recorded on a hard disk through an analog-to-digital (A/D) converter (PXI-5105, National Instruments Corp.) under the control of LabVIEW program. Since the A/D converter has 16 separate channels, the processed AE signals were digitized with 0.1 μ s sampling time and had 2048 samples in the record length for each event for each sensor. The dead time was set after recording an event to 1 ms, to prevent the hard disk from recording too much noise caused by ringing, which is the vibration following a large AE event. The recording of an AE event was triggered when one of the signals from the 16 AE sensors exceeded 3 V. In addition, the number of AE events per second was counted for each AE sensor when the signal exceeded 3 V.

The injected fluid pressure was measured Every 0.1 s through transducers (PW-50MPA, Tokyo Sokki Kenkyujo Co., Ltd., with a full scale of 50 MPa and precision of 0.1 MPa) at the top of the packer, and the flat jack pressures in the X, Y, and Z directions through transducers (PW-20MPA with a full scale of 20 MPa and precision of 0.04 MPa) on the connecting pipes of opposing pairs of flat jacks.

The temperature changes were measured by T-type thermocouples, which can measure temperatures from -200 to 400 °C with resolution of 0.5 degree, glued to the injection pipe just above the packer in the hole and at both ends of the section of pipe covered with electric resistance heating ribbon only for SC-CO₂ injection (Figure 2.4).

2.2.4 Observation of Fractures with Fluorescent Resin

After the HF experiment, the tested specimens were over-cored by a bit with a diameter of 68 mm along the central injection hole (Figure 2.6). The over-cored hollow cores were soaked in the thermosetting acrylic resin monomer containing a fluorescent compound under vacuum to allow the resin monomer to penetrate into the induced fractures, and then heated to set the resin in the cores before sectioning.

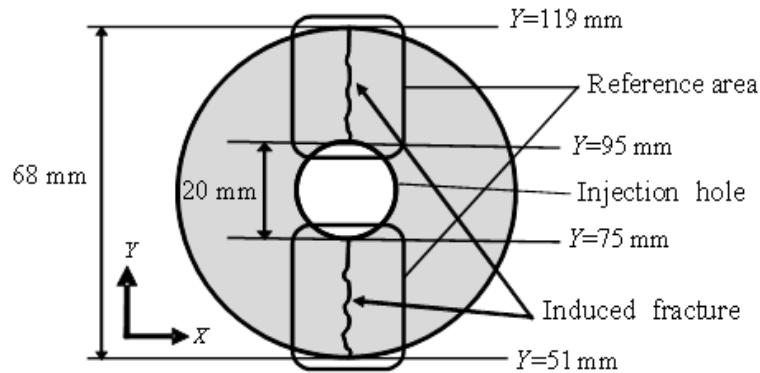


Figure 2.6 Over-cored hollow core for microscopic observation and reference areas on a thin section.

The fractures filled with the resin were visualized and observed under the ultraviolet light irradiation (Nishiyama and Kusuda, 1994). Two thin sections including hydraulically induced fractures were made on the plane where $Z = 85$ mm, corresponding to the center of the pressuring section. No secondary fractures caused by preparing the thin sections were detected because the above-mentioned pre-treatment was completed before sectioning.

2.3 Results

The experimental conditions and the results of the experiments are summarized as in Table 2.2 and Table 2.3 respectively. Because the two tested specimens for each fluid

showed similar trends, the results for only one specimen per fracturing fluid are shown. These specimens are G1115 for SC-CO₂, G1213 for L-CO₂, G1102 for water and G1114 for viscous oil (open circles in the Table 2.3).

Table 2.2 Summary of granite HF experimental conditions.

Specimen (no.)	Fracturing fluid	Temperature (°C)	Viscosity (mPa·s)
G1115	SC-CO ₂	35.5	0.051
G1202	SC-CO ₂	38.4	0.053
G1213	L-CO ₂	12.8	0.097
G1209	L-CO ₂	6.0	0.108
G1102	Water	31.4	0.774
G1103	Water	30.5	0.788
G1114	Oil	11.1	316.0
G1112	Oil	10.6	336.6

Table 2.3 Summary of granite HF experiments results.

	Specimen (no.)	Breakdown pressure P_b (MPa)	Apparent Tensile strength, T (MPa)*	No. of AE sources	L_{av} (mm)	Fractal dimension	Ratio of compression (%)	Tortuosity L/L_0	Average no. of branches
○	G1115	9.10	6.10	118	12.06	2.42	51.30	1.109	2.131
	G1202	10.16	7.16	218	11.44	2.40	62.70	1.075	2.083
○	G1213	11.96	8.96	160	10.78	2.17	54.21	1.120	1.870
	G1209	11.98	8.98	81	12.52	2.15	54.80	1.102	1.927
○	G1102	12.96	9.96	116	8.15	2.20	56.67	1.095	1.789
	G1103	13.33	10.33	72	9.35	2.42	61.42	—	—
○	G1114	23.07	20.07	73	7.39	2.01	69.01	1.062	1.704
	G1112	25.05	22.05	62	8.51	1.96	72.11	1.054	2.029

* Tensile strength is obtained from the equation (3), $T = (1 + \alpha)P_b - 3$, when $\alpha = 0$.

The results discussed are for only specimens marked with open circles (one specimen per fracturing fluid)

2.3.1 Changes in Fluid Pressure and AE Count Rate

Figure 2.7 shows the changes in injected fluid pressure, confining pressure, and AE count rate during injection of SC-CO₂, L-CO₂, water, and viscous oil into the specimen.

The temperature is shown only for SC-CO₂. In the injection of SC-CO₂ and L-CO₂, since CO₂ was fed from the bomb, the bomb pressure around 5 MPa applied in the hole just after the experiments have started. In contrast, in the injection of water and oil, the pressure increased gradually from zero. In all cases, the return pipe was shut after filling the fluids in the dry empty pressurizing section in the hole, and the injection of fluids were maintained at a constant flow rate of 10 mL/min through the experiments. The elapsed time along the lateral axis is taken as zero when the breakdown pressure, which is defined as the peak pressure just before large sudden pressure drop, is recorded.

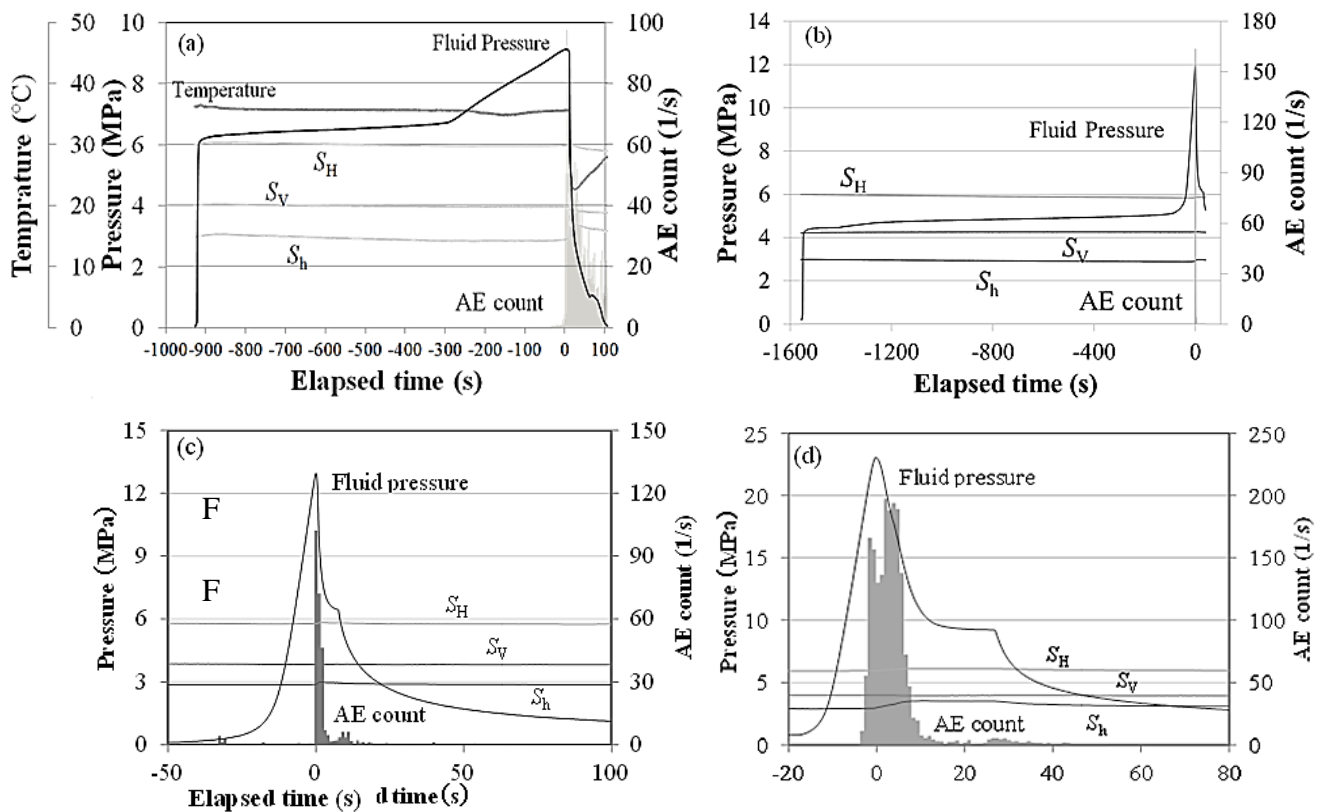


Figure 2.7 Changes in injected fluid pressure, confining pressure, and AE count rate for (a) SC-CO₂, (b) L-CO₂, (c) water, and (d) viscous oil. The temperature change is only shown in (a). The scales of the vertical and horizontal axes differ between plots.

Figure 2.7(a) for the case of SC-CO₂ injection, shows the temperature measured with a thermocouple glued on the injection pipe just above the packer in the hole. The temperature most likely indicates the CO₂ temperature, since the temperature always showed the same temperature measured at the both ends of the section of pipe covered with electric resistance heating ribbon (Figure 2.4) even when the sudden temperature

change of the CO₂ was induced. Since the temperature shows around 36 °C, the test began with the CO₂ in the gas state in the borehole, referring to the phase diagram of CO₂ shown in Figure 2.5. The CO₂ should start transforming into a supercritical state once the fluid pressure get closer to around the critical pressure, 7.38 MPa. This change could be inferred from the change in the increase rate of the fluid pressure under the constant flow rate as shown with the arrow in Figure 2.7(a). This change was most likely caused by the decrease of the fluid compressibility due to the change from the gas to the supercritical state of CO₂.

The fluid pressure decreased sharply to zero just after breakdown at 9.10 MPa. The pressure and temperature, 35.5 °C, at the breakdown demonstrate that the HF was induced by CO₂ of a supercritical state. The pressure decrease, which was caused by leakage through induced fractures, most likely changed the CO₂ from supercritical to gas state again. The temperature also decreased to 22.6 °C just after breakdown, and came back to 27.9 °C at 100 s after the breakdown.

The temperature decrease was probably caused by adiabatic expansion of CO₂, because the measured temperature decrease from 35.2 to 22.6 °C can be induced by 1.15 times larger expansion of the sealed volume of gas state CO₂, under an assumption of simple adiabatic expansion using Poisson's law.

The AE count rate (average of the 16 AE sensors) increased sharply just after breakdown and events continued to occur for several tens of seconds. The confining pressures, S_H , S_V , and S_h (Figure 2.1), were kept nearly constant at 6, 4, and 3 MPa, respectively, with small fluctuations due to fracture growth during breakdown.

As shown in Figure 2.7a-d, breakdown pressure was positively correlated with viscosity of fracturing fluids: 9.10 MPa for SC-CO₂, 11.96 MPa for L-CO₂, 12.96 MPa for water, and 23.07 MPa for viscous oil.

2.3.2 AE Source Locations

As a source location method, the iterative method with the least square principle was used. The method is called Geiger's method (Geiger, 1910; 1912) following the

classification by Ge (2003a; 2003b). Considering the anisotropy of the P wave velocity (Rothman et al., 1974), which was measured before the experiment shown in Table 2.1, the AE source locations were determined within an expected accuracy of several millimeters. This was possible because the chosen AE events satisfy the following criteria (Ishida and Sasaki, 2011): (i) five or more P wave arrival times could be read; and (ii) the standard deviation and the maximum of residuals of arrival times were within 3 μ s. Wave forms of a typical AE event induced by HF with SC-CO₂ illustrating P wave arrival are shown in Figure 2.8.

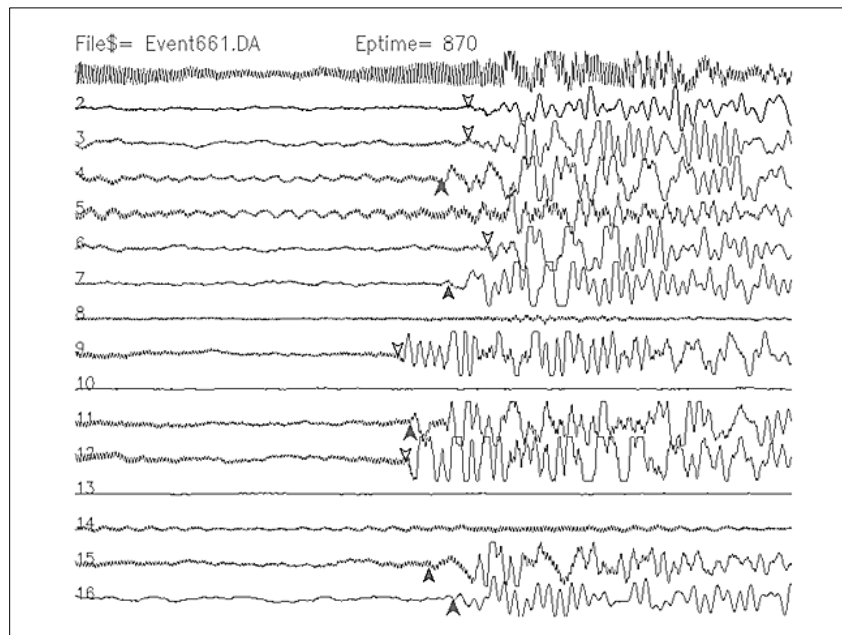


Figure 2.8 P wave first motion arrivals of AE event induced by HF with SC-CO₂. The closed triangles indicate compression in P wave first motion showing upward trace while open triangles indicate dilatation.

Figure 2.9 shows the locations of AE sources observed during the fluid injections projected onto the three orthogonal planes (*XY*, *YZ*, and *ZX*). All of the AE occurred within 15 s after breakdown.

The number of sources that satisfied the conditions mentioned before was 118 for SC-CO₂ (Figure 2.9a), 160 for L-CO₂ (Figure 2.9b), 116 for water (Figure 2.9c), and 73 for viscous oil (Figure 2.9d). Figure 2.9 also shows the fractures visible on the original surfaces of the cubic specimens with the located sources. Fractures were visible on the

two opposite surfaces of the XY plane for SC-CO₂ (Figure 2.9a), the XY and ZX planes for L-CO₂ (Figure 2.9b), and the ZX plane for viscous oil (Figure 2.9d). The fractures contained in the two parallel planes are distinguished by using dark lines (near planes; $Z=170$ mm for the XY and $Y=0$ mm for the XZ planes) and light lines (far planes; $Z=0$ mm for the XY and $Y=170$ mm for the XZ planes). The other fractures were visible on one plane only, while no visible fracture appeared on the YZ planes.

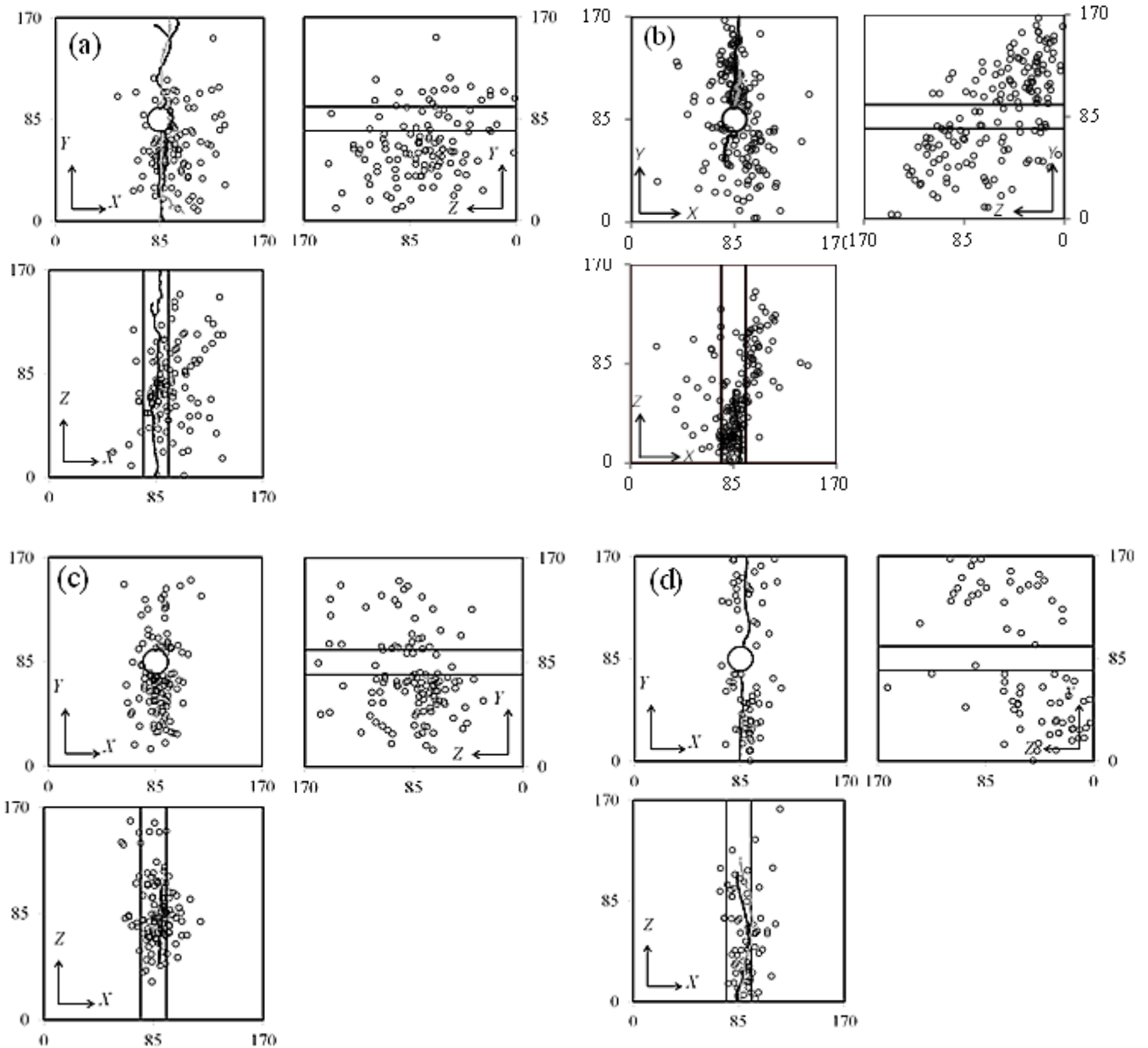


Figure 2.9 AE source distribution and fractures visible on the specimen surface for (a) SC-CO₂, (b) L-CO₂, (c) water, and (d) viscous oil. Dark and light lines show fractures that appeared in different planes facing each other.

The AE sources were distributed along the fractures, as expected from the observed surface fractures. However, the AE sources in Figure 2.9a were more widely distributed rather than lying along a flat plane; this effect seemed to increase with the decrease of viscosity of the fracturing fluids.

To present the differences quantitatively, the maximum likelihood flat plane for the AE distribution was first estimated for each specimen by minimizing the sum of squares of the distances from a source to the flat plane. After that, the average distance, L_{av} , from a source to the maximum likelihood plane was obtained. For the AE distributions shown in Figure 2.9, the L_{av} values were 12.06 mm for SC-CO₂, 10.78 mm for L-CO₂, 8.15 mm for water, and 7.39 mm for viscous oil.

The fractal dimension of the AE distributions was also obtained with the correlation function method, following Hirata et al. (1987) and Grassberger (1983). Theoretically, the fractal dimensions of an infinite number of points distributed on a line, on a plane, and in three-dimensional space are one, two, and three, respectively. However, because the number of distributed points is finite, the fractal dimensions obtained by this method tend to be slightly lower than their respective dimensions (Ishida et al., 1998). Nevertheless, fractal dimension is useful for characterizing the features of the AE distribution, and a larger fractal dimension suggests more extensive fracturing in three dimensions. For the AE distributions shown in Figure 2.9, the fractal dimensions for SC-CO₂, L-CO₂, water, and viscous oil were 2.42, 2.17, 2.20, and 2.01, respectively. This suggests that a low-viscosity fracturing fluid such as SC-CO₂ induces fracturing in three dimensions rather than in two by, for example, forming sinuous fractures with a greater number of secondary branches.

2.3.3 Induced Fracture Patterns Observed with the Fluorescent Method

The fractures induced by HF in the experiments were subtle in all cases, and they were barely identified by tracing segments where the fracturing fluid leaked on the surfaces of the specimens, although they were observed more clearly the more viscous the fracturing fluid. Even after over-coring with a 68 mm diameter around the 20 mm diameter injection hole, the over-cored hollow core still had substantial strength and did

not fail or break into two or more pieces in almost of all cases, as seen in the experiments by Schmitt and Zoback (1992, 1993).

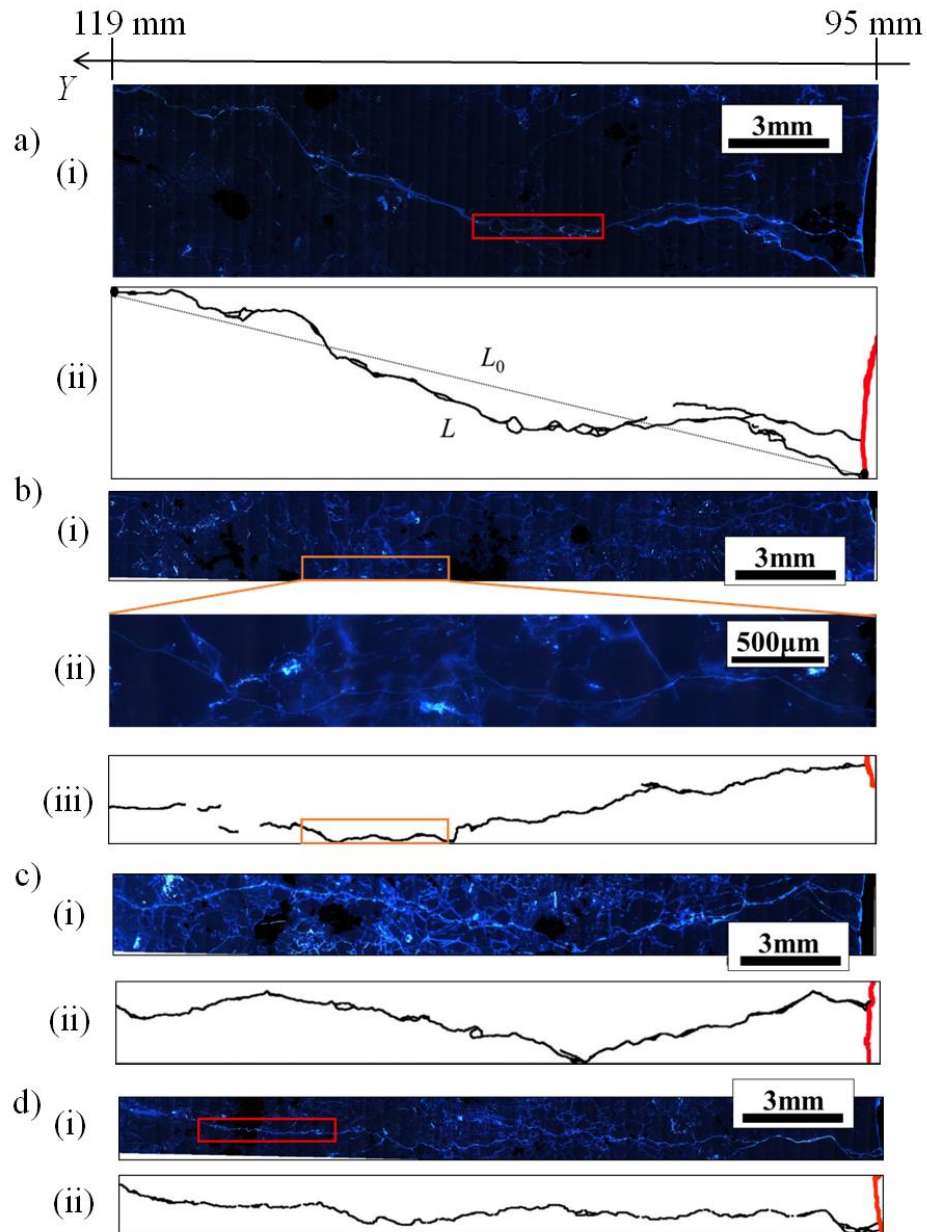


Figure 2.10 Fracture propagation patterns observed on thin sections using the fluorescent method from 95 to 119 mm in the Y -coordinate in Figure 2.6. Specimens fractured by (a) SC- CO_2 (G1115), (b) L- CO_2 (G1213), (c) water (G1102), and (d) viscous oil (G1114). The upper panels show the photo taken of the thin section. The lower panels show sketches of the main fracture, and the red line on the right side indicates the periphery of the injection hole. In (b), an enlarged photo of area enclosed with the orange box is also shown to help identify the main fracture. Fractures in the red boxes in (a) and (d) are shown on the microphotos taken under polarized light in Figure 2.11. The symbols L_0 and L in (a) show the lengths to calculate the tortuosity, L/L_0 , shown in Figure 2.12e.

Figure 2.10 shows fractures propagation patterns observed on the thin sections cut from the hollow cores after being soaked in the acrylic resin containing a fluorescent compound. Although preliminary observations, except for the L-CO₂ injection, have already been reported (Chen et al., 2015), the fracture patterns were examined in relation to the results of AE monitoring.

The upper panels in Figure 2.10 show fluorescent images of the thin section taken under ultraviolet light (Nishiyama and Kusuda, 1994). The bright and bluish-white regions correspond to fractures. The lower panels show sketches of the main fracture induced by the injection. The fracture propagates from right to left in all figures. The periphery of the injection hole is shown with a red line on the right side of the sketch.

The observed area corresponds to the area from *Y* coordinate of 95 to 119 mm in Figure 2.6, and the left side almost corresponds to the inner wall of the over-coring hole. The sketch was made by connecting segments of the main fracture identified with the fluorescence method under ultraviolet light, considering the continuity in the direction of the fracture propagation.

Although it was easy to identify the main fractures in the photos of SC-CO₂, water and viscous oil (Figures 2.10a (i), 2.10c (i) and 2.10d (i)), it is difficult only in the photo of L-CO₂ (Figure 2.10b (i)); therefore, an enlarged photo is used (Figure 2.10b (ii)). The sketches of the main fractures in Figures 2.10a (ii), 2.10b (iii), 2.10c (ii) and 2.10d (ii) show that the fractures are tortuous and never propagate straight, although they propagate along the direction of the maximum compressive stress and along the rift plane where the main pre-existing micro fractures align. Fluids with lower viscosity induce fractures with higher tortuosity, because intermittent and stepwise fracture extensions become more conspicuous.

To examine the correlations between fracture patterns and the constituent mineral grains of the specimens, photomicrographs of the fracture patterns on thin sections for SC-CO₂ and oil injection in the boxes in Figure 2.10 were taken using a petrographic microscope in crossed-polarized light (crossed Nicols). The fractures induced by SC-CO₂ propagate mainly along the grain boundaries of the constituent minerals (Figure 2.11a).

In contrast, Figure 2.11b shows that the fractures induced by oil cut through many mineral grains. This is most likely a reason why the fracture pattern depends on the viscosity of the fracturing fluid.

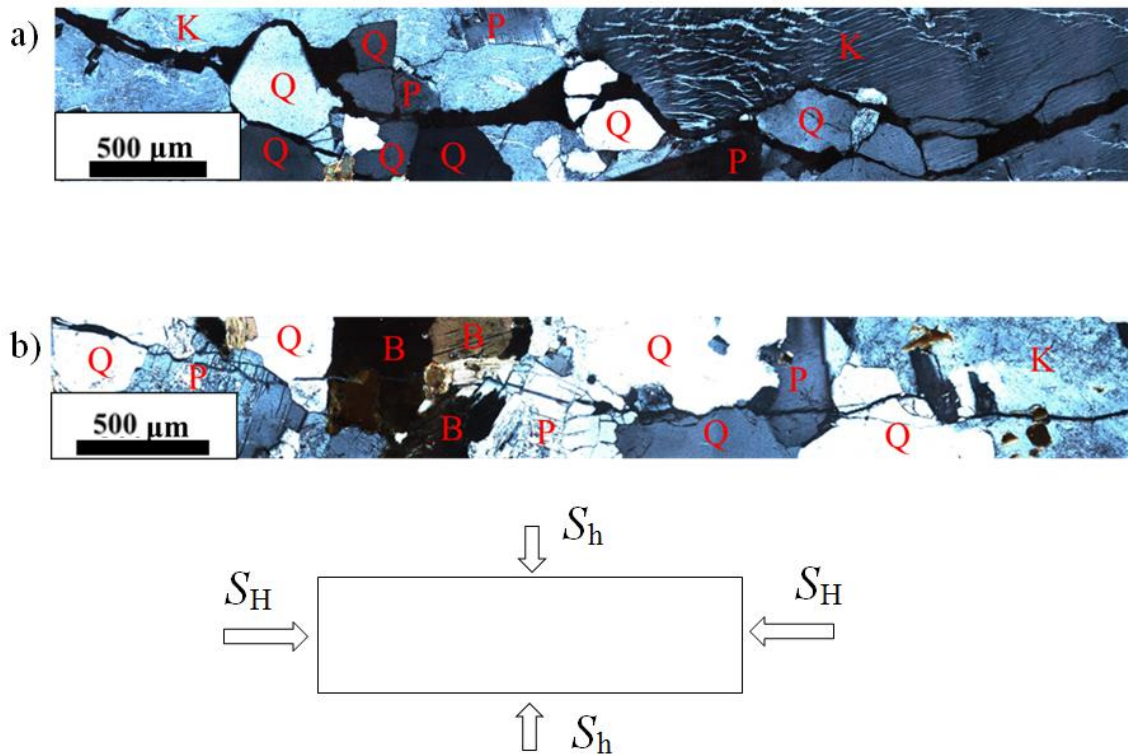


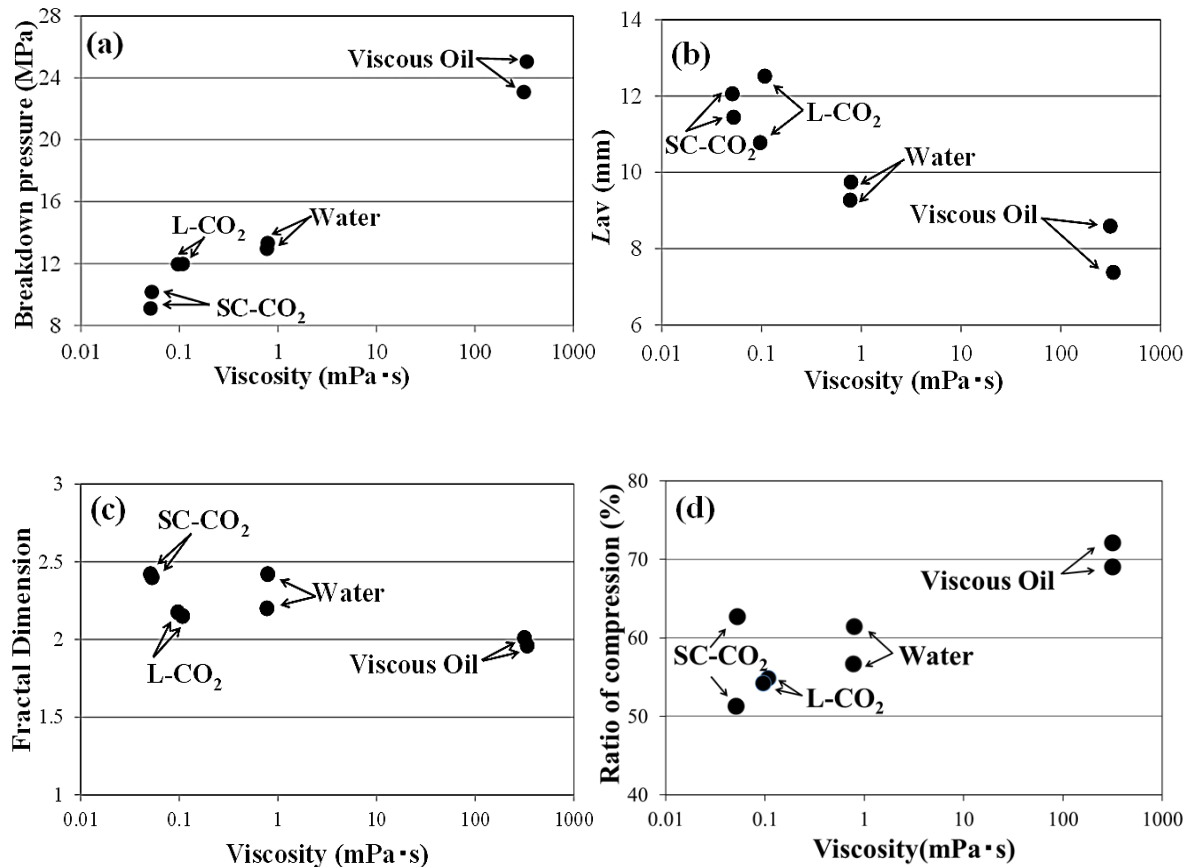
Figure 2.11 Observation on fracture patterns and constituent mineral grains for (a) SC-CO₂ injection, red box in Figure 2.10a, and (b) oil injection, red box in Figure 2.10d, using a petrographic microscope in crossed-polarized light (crossed Nicols). (B: biotite, K: K-feldspar, P: plagioclase and Q: quartz.) The bottom figure illustrates the stress condition when the fractures extended in the specimen.

Fracture aperture shown in Figure 2.11a is larger than that in Figure 2.11b, although Ishida et al. (2004) and Stanchits et al. (2014) showed that the higher viscosity fracturing fluid tends to induce fractures having larger aperture. Ishida et al. (2004) injected water and viscous oil into blocks of *Kurokami-jima* granite with monitoring pressure change of the flat jacks applying the confining pressure. Stanchits et al. (2014) injected two kinds of silicon oil having thousand-fold different viscosity into low permeability blocks of *Colton* sandstone with monitoring volume of the injected fluid. Their results both indicated that the higher viscosity tends to induce the larger aperture

fractures, which is inconsistent with the results shown in Figure 2.11. Although the changes of the flat jack pressure and the injected volume were not monitored, the large aperture observed in the SC-CO₂ injection was probably caused by expansion of CO₂ with the phase change from SC-CO₂ to gas due to the pressure decrease after the fracture extension to the lateral free surface of the specimen.

2.4 Effect of Fluid Viscosity

Figure 2.12 shows the dependency on the fracturing fluid viscosity of breakdown pressure, the AE distribution, and fracturing mechanism based on ratios of the P wave first motion polarity of AE events and the fracture features observed by the fluorescence method. To confirm the generality of the properties, Table 2.3 shows the data for the chosen specimens described in the previous section and for the alternate specimens G1202 for SC-CO₂, G1209 for L-CO₂, G1103 for water, and G1112 for viscous oil.



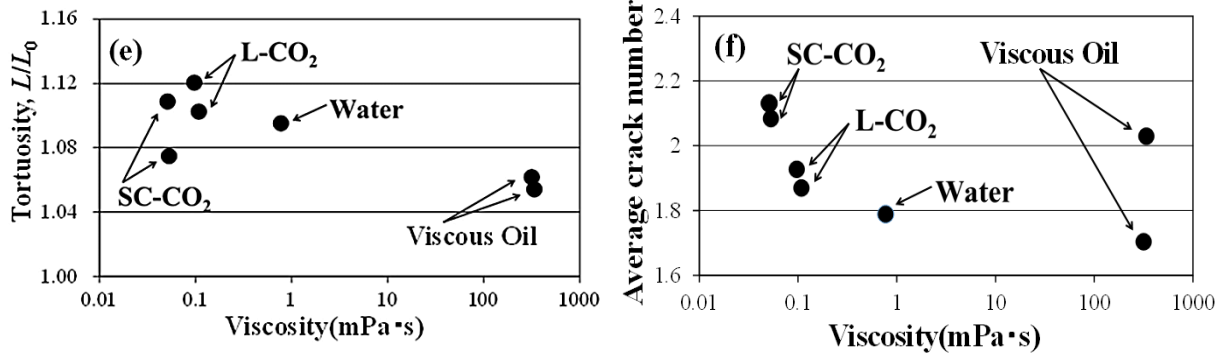


Figure 2.12 Effect of fracturing fluid viscosity on (a) breakdown pressure, (b) average distance L_{av} from a source to the estimated most likely plane, (c) fractal dimension, (d) the compression ratio to the total number of the polarities in P wave first motion, (e) fracture tortuosity, and (f) average fracture number. The results in (a)–(d) were derived from AE data, whereas the results in (e) and (f) were from microscopic fracture observation using the fluorescent method.

The viscosities of SC-CO₂ and L-CO₂ in Figure 2.12 were estimated from the temperature and pressure at the breakdown point, following the equation of state for CO₂ implemented by Ohmori (<http://hp.vector.co.jp/authors/VA030090/>) based on the theory by Fenghour et al. (1998). The viscosities of the water were obtained from Chronological Scientific Tables (National Astronomical Observatory of Japan, 1995), and those of the oil were obtained from a table provided by the oil manufacturer, by using the temperatures measured during the experiments.

2.4.1 Breakdown Pressure and Apparent Tensile Strength

Figure 2.12a shows the dependency of breakdown pressure on fracturing fluid viscosity. This figure clearly shows that breakdown pressure increases with viscosity. The tendency is consistent with the experimental results by Morita et al. (1996) using water-base and oil-base muds, and in addition, the numerical simulation by Bungler et al. (2010).

Schmitt and Zoback (1992, 1993) discussed carefully the effect of pore pressure on fracture initiation of HF through laboratory experiments using hollow cylinder of westerly granite and glass, where they changed the pressurization rate and the magnitude

of the confining pressure applied on the outer surface of the cylinder. Here the effect is discussed in much simpler way than Schmitt and Zoback (1992, 1993), using the following equation proposed by Scheidegger (1962) for a vertical borehole;

$$P_b = 3S_{h_{min}} - S_{H_{max}} + T - P_p \quad \text{----- (1)}$$

Where P_b : the breakdown pressure, P_p : the pore pressure, T : the tensile strength, $S_{h_{min}}$: the minimum horizontal stress and $S_{H_{max}}$: the maximum horizontal stress.

In the experiments discussed in this chapter, $S_{h_{min}}$ and $S_{H_{max}}$ correspond to S_h and S_H respectively as shown in Figure 2.1. By putting that $S_{h_{min}} = S_h$, $S_{H_{max}} = S_H$ and $P_p = \alpha P_b$, the equation (1) becomes;

$$T = S_H - 3S_h + (1 + \alpha)P_b \quad \text{----- (2)}$$

The case that $\alpha = 0$ corresponds to the state that no pore pressure is applied prior to the infiltration of fracturing fluid, while the case that $\alpha = 1$ corresponds to the state that the pore pressure is equal to the fracturing fluid pressure applied on the wall of the injection hole. The magnitude of S_h fluctuated at the breakdown, because a specimen expanded in the X direction, due to intrusion of fracturing fluid into a fracture induced along the Y direction, and resulted in pushing the flat jacks applying the confining pressure, S_h . However, since the fluctuation is not too large as shown in Figure 2.7, by substituting 3 MPa for S_h and 6 MPa for S_H , the equation (2) becomes;

$$T = (1 + \alpha)P_b - 3 \quad \text{----- (3)}$$

The apparent tensile strength, T , obtained from the equation (3) is shown in Table 2.3 for the cases that $\alpha = 0$. Even in the case that $\alpha = 0$, the apparent tensile strength, T , increases from 6 to 22 MPa, which is much larger than Brazilian tensile strength of the *Kurokami-jima* granite, 3.38 MPa. In the case that $\alpha = 1$, the apparent tensile strength, T , increases to even larger values.

In Brazilian test, the tensile stress uniformly distributes along the fracture plane, while in our HF experiment, the tensile stress in the circumference direction is the largest on the wall of the injection hole and decreases with the square of the distance from the center of the hole (Kirsch, 1898). When the difference of the stress distribution is taken

into account by introducing a concept of “risk of rupture” proposed by Weibull (1939a, 1939b) under the assumption of uniform distribution of Griffith fractures, the breakdown pressure, P_b , becomes 1.45 times larger than that of the Brazilian tensile strength (Ishida et al., 2005). The difference of 1.45 times showed good agreement with that of 1.47 obtained in their experiments (Ishida et al., 2005). However, the difference is still small to explain the difference between the apparent tensile strength and the Brazilian tensile strength.

In this study, the fractures induced in the HF experiments seemed to extend instantaneously to the lateral surface of the specimen. Discussion on the fracture extension considering the stress intensity factors at a fracture tip, as described by Ishida et al. (1997) following Zoback et al. (1977) and Zoback and Pollard (1978), may help to interpret the difference in the apparent tensile strength depending on the viscosity of the fracturing fluid.

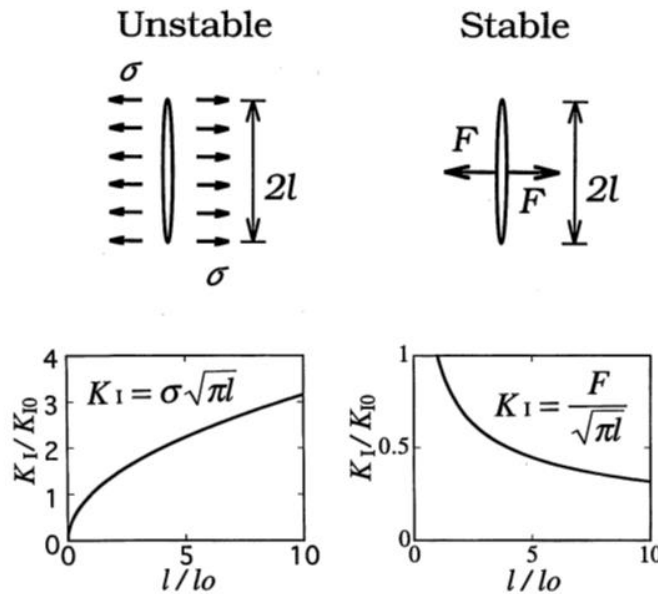


Figure 2.13 Stable and unstable fracture growth from a viewpoint of stress intensity factor of mode I at a fracture tip. (After Ishida et al. (1997) following Zoback et al. (1977) and Zoback and Pollard (1978))

The left side of Figure 2.13 depicts the case in which hydrostatic pressure, σ , applies throughout an ellipsoidal fracture surface. In this case, $K_I = \sigma(\pi l)^{1/2}$, where K_I is

the stress intensity factor of mode I at a fracture tip and l is half of the fracture length. According to this relation, the stress intensity factor at a fracture tip increases with fracture length; in other words, a fracture never stops once it starts to extend. The right of Figure 2.13 depicts the case in which a pair of point loads, F , is applied at the center of an ellipsoidal fracture. In this case, $K_I = F(\pi l)^{-1/2}$, which indicates that stress intensity factor at a fracture tip decreases with fracture length; that is, a fracture never extends without an additional increase in applied loads.

It can be expected that the fracturing fluid pressure is localized closer to the fracture tip, the lower the viscosity of the fluid used. Thus, the low viscosity fluid injection would make state close to that hydrostatic pressure, σ , applied along an ellipsoidal fracture surface, while the high viscosity fracturing fluid injection would result in a state analogous to that of a pair of point loads, F , applied at the center of an ellipsoidal fracture. Consequently, the difference of the apparent tensile strength, T , in other words, the difference of the breakdown pressure, P_b , among the fracturing fluids, is most likely caused by the differences of their viscosity.

From the discussion above, in field operations for the same rock type stratum under the same in situ stress condition and flow rate, the breakdown pressure for injecting a low-viscosity fluid, such as SC-CO₂, is expected to be lower than that of water and much lower than that of high-viscosity fluid such as gel.

2.4.2 AE Distribution

Figure 2.12b shows the dependency on viscosity of the average distance, L_{av} , from a source to the maximum likelihood plane. This figure clearly indicates that L_{av} decreases with viscosity. This suggests that low-viscosity fracturing fluids induce fractures that propagate further away from a flat plane, whereas viscous fluids, such as gels, tend to induce fractures along a flat plane. Figure 2.12c shows that the fractal dimension, FD , of the AE distributions decreases with viscosity, suggesting that low-viscosity fracturing fluids induce fractures that propagate three-dimensionally, rather than two dimensionally along a flat plane.

2.4.3 Fracturing Mechanism Deduced from P Wave Polarity of AE

The differences in the fracture features possibly arose from a difference in fracturing mechanism. Thus, by comparing the ratios of the P wave first motion polarity of approximately 30 AE events that were detected by at least seven sensors, allowing P wave arrivals to be determined for a source location.

A calibration test, in which a small steel ball was dropped onto the upper surface of a thick steel plate and the resultant wave forms were recorded by sensors glued onto the plate's lower surface, showed that compression corresponded to an upward trace and dilation to a downward trace.

On Figure 2.8, the closed triangles indicate compression in P wave first motion showing upward trace while the open triangles indicate dilatation. For example, in the case of Figure 2.8, since the number of compression is five and that of dilatation is five, the compression ratio in P wave first motion for this AE event becomes 50%.

Figure 2.12d shows the compression ratio in P wave first motion tends to increase with viscosity. The ratio would be 50% for a pure shear fracture and 100% for a pure tensile fracture. Thus, the results suggest that a low-viscosity fracturing fluid tends to induce shear dominant fractures, whereas viscous fluids tend to induce tensile dominant fractures.

As shown in Figure 2.11a, the fractures induced by SC-CO₂ propagate mainly along the grain boundaries of the constituent minerals, producing many small fractures inclined in the direction of the maximum compressive stress, S_H , which is the propagating direction of a main fracture. As shown in Figure 2.9, the induced main fractures extended in planes almost parallel to the Z direction (the direction of the intermediate principal stress, S_V) in all experiments and we observe the fractures on XY plane normal to the Z direction in Figure 2.11a. Thus, ignoring effect of the intermediate principal stress and considering the two dimensional stress conditions, because shear stress develops on a plane inclined in the direction of the maximum compressive stress, S_H , the inclined fractures are easy to be induced by shear fracture.

In contrast, Figure 2.11b shows that the fractures induced by viscous oil injection cut through many mineral grains and propagate almost straight along the direction of the maximum compressive stress without bending. Because shear stress does not develop on a plane parallel to the direction of the maximum compressive stress, the fractures are probably induced by tensile fracture rather than by shear. In addition, in the oil injection, because the fractures extended to the both lateral surfaces of the specimens as shown in Figure 2.9d and the injected oil seeped out from the induced fractures on the specimen surfaces, the tensile fractures are most likely induced by the intrusion of the viscous oil.

2.4.4 Fracture Features Deduced from Microscopic Observation

Figure 2.12e shows the dependency on viscosity of the tortuosity, L/L_0 , where L is the fracture length measured by connecting 0.05 mm long line segments, namely a divider, along the main fracture, and L_0 is the length of the straight line from the initiation point of the fracture on the wall of the injection hole to its end point on the inner wall of the over-coring (Figure 2.10a).

The main fractures are traced in both directions from the fracturing hole, from Y coordinates of 75 to 51 mm and from 95 to 119 mm (Figure 2.6). The tortuosity for each specimen is the average of the tortuosities obtained in the two opposite directions. Although the results for the two specimens for each fracturing fluid are plotted, only one result is plotted for the water injection. This is because the fractures in specimen G1103 for water injection could not be filled with the fluorescent resin and no observation was obtained. The tortuosity of the induced fractures tended to increase with the decrease of fracturing fluid viscosity, which is consistent with the fracture propagation patterns in Figure 2.10.

Figure 2.12f shows the dependency on viscosity of an average of the fracture numbers, which were counted when the induced fractures crossed the scanning lines at intervals of 1 mm from the injection hole to the inner wall of the over-coring. The fractures were counted excluding preexisting fractures, voids, and other defects with checking the propagation direction and continuity of the fractures through careful observation of fracture width, fluorescent resin brightness, and constituent mineral grains

under polarized and ultraviolet light. The fractures were counted in the two opposite directions from the fracturing hole, and the number plotted is the average obtained in the both directions. Thus, the number corresponds roughly to an average number of fracture branches. The number of induced fractures increased with the decrease in fluid viscosity, although the number is large for oil injection in specimen G1112. This is an exceptional case, because the observation of this specimen showed that one of the main fracture propagations was obstructed by a large biotite grain near the injection hole and the fracture branches were in many directions.

The trends in Figures 2.12e and 2.12f are consistent with those obtained from the AE distribution, where the average distance, L_{av} , and the fractal dimensions, FD , increased with the decrease of fluid viscosity (Figures 2.12b and 2.12c).

2.5 Discussion

Previously, Ishida et al. (2004) conducted HF experiments on the same kind of cubic granite as in the present study by using water and viscous oil, which showed similar fracture features and fracture mechanism. Ishida et al. (2012), Kizaki et al. (2013) and Stanchits et al. (2014) suggested the same dependency on the viscosity of the fracturing fluid, including SC-CO₂, based on their similar experiments using granite, tuff, sandstone, and shale. Shimizu et al. (2011) simulated HF using their Distinct Element Method code, and provided a persuasive interpretation for the dependency of the breakdown pressure, AE fracturing mechanism, and fracture features on fluid viscosity.

In actual reservoirs, Warpinski et al. (2005) and Dinske et al. (2010) in tight gas reservoirs and Baria and Green (1986) in geothermal field made comparative analyses of micro seismicity induced by HF using viscous fluid and water. Baria and Green (1986) and Dinske et al. (2010) could not show clear difference between the two fluids, while Warpinski et al. (2005) showed that slick water fracturing extends a much larger area further in three dimensions than gel fracturing, which is consistent with the findings from this study laboratory experiments. In actual field operations of HF, weak planes, such as preexisting fractures, sedimentary planes and defects in strata, may behave in a similar manner to grain boundary in the granite specimens.

These experiments concluded that HF using low-viscosity fracturing fluid tends to induce shear dominant fracture resulting in extensive three-dimensional fracturing rather than the two-dimensional fracturing observed for high-viscosity fluid. The three-dimensional fractures, which tend to be sinuous and have many secondary branches, could be expected to form pathways favorable for shale gas recovery, EGS and other processes. In this point of view, CO₂ fracturing is better than conventional water fracturing for these purposes.

In actual field operations of HF, a solid material called proppant, typically treated sand or man-made ceramic materials, is usually injected into the induced fractures to prevent them from closing due to rock stresses. However SC-CO₂ has little ability to transport the proppant due to its low viscosity. In addition, since CO₂ is more corrosive than water to steel pipes and other units, this nature of CO₂ may make troubles in actual HF operations. For the first problem, it may be better to inject L-CO₂, due to its larger viscosity than SC-CO₂, through a double pipe, making vacuum in a space between the inner and outer pipe to prevent it from heating underground. In another way, if it is possible to make a new type proppant to solve into SC-CO₂ and to deposit in the fractures due to phase change of CO₂ caused by the decrease of pressure and temperature with the breakdown, the problem would be solved. For the second problem, since CO₂ injection is usually used for enhance oil recovery in the petroleum industry, the experiences would help to solve the problem.

CO₂ fracturing most likely form pathways favorable for shale gas recovery and heat extraction, where large amounts of CO₂ would remain underground distributed across many wells even if only a small amount of CO₂ is used in each well injection. Thus, by overcoming the problems for field application of this approach, CO₂ fracturing for shale gas recovery and heat extraction from EGS could result in economically viable CO₂ sequestration.

2.6 Conclusions

Reproducible HF experiments were conducted in 170 mm cubic granite specimens with a 20 mm diameter central hole using SC-CO₂, L-CO₂, water, and viscous oil with viscosities from 0.051 to 336.6 mPa·s.

Based on the dependency on fracturing fluid viscosity of the breakdown pressure, AE distribution, the fracturing mechanism deduced from ratios of the P wave first motion polarity of AE events, and fracture features observed by the fluorescent method, the following conclusions can be drawn:

(1) The breakdown pressure increases with viscosity, which is consistent with previous experiments and numerical simulations. Thus, the breakdown pressure with the injection of a low-viscosity fluid, such as SC-CO₂, was expected to be lower than that of water, and much lower than that of viscous fluid such as gel used in field operations.

(2) AE source distributions clarified that the average distance, L_{av} , from a source to the maximum likelihood plane and the fractal dimensions, FD , of the source distributions increased with the decrease in fluid viscosity. This suggests that HF using low-viscosity fluid tends to induce extensive three-dimensional fracturing rather than the two-dimensional fracturing observed for high-viscosity fluid.

(3) Ratios of the P wave first motion polarity suggest that a low-viscosity fracturing fluid tends to induce shear dominant fracture, whereas viscous fluids tend to induce tensile dominant fracture.

(4) The photomicrographs taken using a petrographic microscope in crossed-polarized light (crossed Nicols) show that the fractures induced by SC-CO₂ propagated mainly along the grain boundaries of the constituent minerals, and consequently, many small fractures inclined in the direction of the maximum compressive stress were observed. In contrast, the fractures induced by viscous oil injection cut through the many mineral grains and propagated almost straight along the direction of the maximum compressive stress without bending. Because shear stress developed on a plane inclined in the direction of the maximum compressive stress, the inclined fractures were probably

induced by shear fracture. Thus, the observation was consistent with the results obtained from AE monitoring, that is, shear dominant fracturing occurred with low-viscosity fluid injection, whereas tensile dominant fracturing occurred with high-viscosity fluid injection.

(5) The microscopic fracture observations showed that the tortuosity of a main fracture and the average number of fractures increased with the decrease in fluid viscosity. This observation was consistent with the results of AE monitoring.

(6) The observed dependency of fracture features on the fracturing fluid viscosity was consistent with those reported in previous laboratory experiments, numerical simulations, and with the field micro seismic maps associated with the injection of water and gel.

(7) These results suggest that CO₂ fracturing induces three-dimensionally sinuous fractures with many secondary branches, which seem to be desirable pathways for shale gas recovery, enhanced geothermal systems (EGS) and other processes. By overcoming the difficulty in injecting proppant into induced fractures due to low viscosity of SC-CO₂, CO₂ fracturing could realize economically viable CO₂ sequestration, because large amounts of CO₂ would remain underground distributing across many wells even if only a small amount of CO₂ is used in each well injection.

References

Baria R. and Green A. (1986). Seismicity Induced During a Viscous Stimulation at the Camborne School of Mines Hot Dry Rock Geothermal Energy Project in Cornwall, England. *Progress in Acoustic Emission III*, the Japanese Society of NDI, p. 407–429.

Brown D. (2000). A Hot Dry Rock Geothermal Energy Concept Utilizing Supercritical CO₂ Instead of Water. Paper presented at 25th Workshop on Geothermal Reservoir Engineering, Stanford University. Stanford, California, USA.

Bunger A. and Detournay E. (2008). Experimental Validation of the Tip Asymptotics for a Fluid-Driven Fracture. *Journal of the Mechanics and Physics of Solids*, 56, p. 3101–3115.

Bunger A., Lakirouhani A. and Detournay E. (2010). Modelling the Effect of Injection System Compressibility and Viscous Fluid Flow on Hydraulic Fracture Breakdown Pressure. *Proceedings of the 5th International Symposium on In-Situ Rock Stress*, the International Society for Rock Mechanics, p. 59-67. Beijing, China.

Chen Y., Nagaya Y. and Ishida T. (2015). Observations of Fractures Induced by Hydraulic Fracturing in Anisotropic Granite. *Journal of Rock Mechanics and Rock Engineering*, 48, p. 1455–1461, doi: 10.1007/s00603-015-0727-9.

Dinske C., Shapiro S. and Rutledge J. (2010). Interpretation of Microseismicity Resulting From Gel and Water Fracturing of Tight Gas Reservoirs. *Journal of Pure and Applied Geophysics*, 167, p. 169-182.

Fenghour A., Wakeham W. and Vesovic V. (1998). The Viscosity of Carbon Dioxide. *Journal of Physical and Chemical Reference Data*, 27(1), p. 31–44, doi: 10.1063/1.556013.

Ge M. (2003a). Analysis of Source Location Algorithms--Part I: Overview and Non-Iterative Methods. *Journal of Acoustic Emission*, 21, p. 21-28.

Ge M. (2003b), Analysis of Source Location Algorithms--Part II: Iterative Methods. *Journal of Acoustic Emission*, 21, p. 29-51.

Geiger L. (1910). Herbsetimmung bei Erdbeben aus den Aukunfzeiten. K. Gessell. Will. Goett. 4, p. 331-349 (German).

Geiger L. (1912). Probability Method for the Determination of Earthquake Epicenters from the Arrival Time Only. Bulletin of St. Louis University, 8, p. 60-71.

Grassberger P. (1983). Generalized Dimensions of Strange Attractors. Physics Letters, 97A(6), p. 227–230.

Guo F., Morgenstern N. and Scott J. (1993a). An Experimental Investigation Into Hydraulic Fracture Propagation--Part 1. Experimental Facilities. International Journal of Rock Mechanics and Mining Science & Geomechanics Abstracts, 30, p. 177-188.

Guo F., Morgenstern N. and D. Scott J. (1993b). An Experimental Investigation Into Hydraulic Fracture Propagation--Part 2. Single Well Tests. International Journal of Rock Mechanics and Mining Science & Geomechanics Abstracts, 30, p. 189-202.

Guo F., Morgenstern N. and Scott J. (1993c). An Experimental Study of Well Communication by Hydraulic Fracturing. International Journal of Rock Mechanics and Mining Science & Geomechanics Abstracts,30, p. 203-218.

Haimson B. and Fairhurst C. (1969). Hydraulic Fracturing in Porous-Permeable Materials. Journal of Petroleum Technology, July, 1969, p. 811-817.

Hirata T., Satoh T., and Ito K. (1987). Fractal Structure of Spatial Distribution of Microfracturing in Rock. Geophysical Journal of the Royal Astronomical Society, 90, p. 369–374, doi: 10.1111/j.1365-246X.1987.tb00732.x.

Ishida T., Kitano K., Kinoshita N. and Wakabayashi N. (1990). Acoustic Emission and P Wave Velocity Monitoring During Thermal Cracking in a Locally Heated Granite Block. Journal of Japan Society of Civil Engineers, 418(III-13), p. 153-161 (Japanese with English abstract).

Ishida T. and Sasaki S. (2011). Numerical Simulation to Examine Accuracy of AE Source Location and Its Applications to In-Situ Rock Monitoring. Journal of Acoustic Emission, 29, p. 260–272.

Ishida T., Chen Q. and Mizuta Y. (1997). Effect of Injected Water on Hydraulic Fracturing Deduced from Acoustic Emission Monitoring. *Journal of Pure and Applied Geophysics*, 150, p. 627-646.

Ishida T., Chen Q., Kaieda H. and Mizuta Y. (1998). Fractal Analysis on a Source Distribution of Acoustic Emissions in a Hot Dry Rock Mass Reservoir. *Journal of Japan Society of Civil Engineers*, 536(III-43), p. 49-63 (Japanese with English abstract).

Ishida T., Chen Q., Mizuta Y. and Roegiers J. (2004). Influence of Fluid Viscosity on the Hydraulic Fracturing Mechanism. *Journal Energy Resources Technology*, 126, p. 190–200, doi: 10.1115/1.1791651.

Ishida T., Oka H., Yonehiro N., Tamura Y. and Mizuta Y. (2005). Examination on the Tensile Strengths of Hydraulic Fracturing Using the Probabilistic Theory of Fracture. *Journal of the Mining and Materials Processing Institute of Japan (Shigen-to-Sizai)*, 121, p. 576-582. (Japanese with English abstract)

Ishida T., Miyazaki S., Ishii T., Amemiya K. and Mizuta Y. (2006). Preliminary Results of Air Permeability Test Under Tensile Stress Condition Using a Hollow Cylindrical Rock Specimen. *Proceedings of EUROCK 2006*, p. 127-131. Liege, Belgium.

Ishida T., Aoyagi K., Niwa T., Chen Y., Murata S., Chen Q. and Nakayama Y. (2012). Acoustic Emission Monitoring of Hydraulic Fracturing Laboratory Experiment with Supercritical and Liquid CO₂. *Geophysical Research Letters*, 39, L16309, doi: 10.1029/2012GL052788.

International Society for Rock Mechanics, Commission on Standardization of Laboratory and Field Tests (1979). Suggested Methods for Determining Water Content, Porosity, Density, Absorption and Related Properties and Swelling and Slake-Durability Index Properties. *International Journal of Rock Mechanics and Mining Science & Geomechanics Abstracts*, 16, p. 143-151.

Jansen D., Carlson S., Young R. and Hutchins D. (1993). Ultrasonic Imaging And Acoustic Emission Monitoring of Thermally Induced Microcracks in Lac Du Bonnet Granite. *Journal of Geophysical Research*, 98, p. 22231-22243.

Kirsch C. (1898). Die Theorie der Elastizität und die Bedürfnisse der Festigkeitslehre, Z. Ver. Dtsch. Ing., 42, p. 797–807 (German).

Kizaki A., Ohashi K., Tanaka H. and Sakaguchi K. (2013). Effects of Vertical Stress on Fracture Propagation Using Supercritical Carbon Dioxide. Proceeding of EUROCK, International Society for Rock Mechanics, Paper No. CH149, (ISBN 978-1-138-00080-3). Wroclaw, Poland.

Lin W. (2002). Permanent Strain of Thermal Expansion and Thermally Induced Microcracking in Inada Granite. Journal of Geophysical Research: Solid Earth, 107, B10.

Morita N., Black A. and Fuh G. (1996). Borehole Breakdown Pressure with Drilling Fluids -1, Empirical Results. International Journal of Rock Mechanics and Mining Science & Geomechanics Abstracts, 33, p. 39-51.

National Astronomical Observatory of Japan (1995). Chronological Scientific Tables, Maruzen Publishing, p. 446–447. Tokyo, Japan.

Nishiyama T., and Kusuda H. (1994). Identification of Pore Spaces and Micro Cracks Using Fluorescent Resins. International Journal of Rock Mechanics and Mining Science & Geomechanics Abstracts, 31, p. 369–375.

Pruess K. (2006). Enhanced Geothermal Systems (EGS) Using CO₂ as Working Fluid - A Novel Approach for Generating Renewable Energy with Simultaneous Sequestration of Carbon. Journal of Geothermics, 35, p. 351–367.

Rothman R., Greenfield R. and Hardy H. (1974). Errors in Hypocenter Location Due to Velocity Anisotropy. Bulletin of the Seismological Society of America, 64, p. 1993–1996.

Sano O., kudo K. and Mizuta Y. (1992). Experimental Determination of Elastic Constants of Oshima Granite, Barre Granite and Chelmsford Granite. Journal of Geophysical Research, 97, p. 3367-3379.

Scheidegger A. (1962). Stress in Earth's Crust as Determined from Hydraulic Fracturing Data. Geologie und Bauwesen, 27, p. 45-53.

Shimizu H, Murata S. and Ishida T. (2011). The Distinct Element Analysis for Hydraulic Fracturing in Hard Rock Considering Fluid Viscosity and Particle Size Distribution. *International Journal of Rock Mechanics and Mining Sciences*, 48(5), p. 712-727.

Stanchits S., Surdi A., Gathogo P., Edelman E. and Suarez-Rivera R. (2014). Onset of Hydraulic Fracture Initiation Monitored by Acoustic Emission and Volumetric Deformation Measurements. *Rock Mechanics and Rock Engineering*, 47, p. 1521–1532, doi: 10.1007/s00603-014-0584-y.

Schmitt D. and Zoback M. (1992). Diminished Pore Pressure in Low-Porosity Crystalline Rock Under Tensional Failure: Apparent Strengthening by Dilatancy. *Journal of Geophysical Research*, 97, p. 273-288.

Schmitt D. and Zoback M. (1993). Infiltration Effects in the Tensile Rupture of Thin Walled Cylinders of Glass and Granite: Implications for the Hydraulic Fracturing Breakdown Equation. *International Journal of Rock Mechanics and Mining Science & Geomechanics Abstracts*, 30, p. 289–303, doi: 10.1016/0148-9062(93)92731-5.

Vutukuri V. and Katsuyama K. (1994). *Introduction to Rock Mechanics*, p.125-129, Industrial Publishing & Consulting, Inc., Tokyo.

Warpinski N., Kramm R., Heinze J. and Waltman C. (2005). Comparison of Single- and Dual-array Microseismic Mapping Techniques in the Barnett Shale. paper presented at 2005 Annual Technical Conference and Exhibition, Society of Petroleum Engineers. Dallas, Texas, USA.

Weibull W. (1939a). A Statistical Theory of the Strength of Materials. *Ingeniörs Vetenskaps Akademiens, Handlingar*, 151.

Weibull W. (1939b). The Phenomenon of Rapture in Solid. *Ingeniörs Vetenskaps Akademiens, Handlingar*, 153.

Zhou X. and Burbey T. (2014). Fluid Effect on Hydraulic Fracture Propagation Behavior: A Comparison between Water and Supercritical CO₂-Like Fluid. *Journal of Geofluids*, 14, p. 174–188, doi: 10.1111/gfl.12061.

Zoback M., Rummel F., Jung R. and Raleigh C. (1977). Laboratory Hydraulic Fracturing Experiments In Intact And Pre-Fractured Rock. International Journal of Rock Mechanics and Mining Science & Geomechanics Abstracts, 14, p.49-58.

Zoback M. and Pollard D. (1978). Hydraulic Fracture Propagation and the Interpretation of Pressure-Time Records for In-Situ Stress Determination. Proceedings of 19th US Rock Mechanics Symposium, p. 14-22. Reno, Nevada, USA.

Chapter 3

Fracturing Mechanism in Hydraulic Fracturing of Shale Cores

3.1 Background

The shale gas refers to the natural gas trapped within formations of shale, a fine grained sedimentary rock that can be a rich source of petroleum and natural gas. However, since the low permeability of shale greatly inhibits the flow of gas from reservoir rocks to production wells, the economic viability of developing shale gas depends on effective stimulation of reservoirs. Recently, horizontal wells employing a multistage hydraulic fracturing technique have become the stimulation method of choice and proved successful in shale gas reservoirs (Arthur et al., 2008).

Hydraulic fracturing (HF) is the process of initiation and propagation of fractures by injection of a fluid at a pressure higher than the failure stress of the rock. The technique of hydraulic fracturing stress measurements was developed by Hubbert and Willis (1957). Building on this work, Cleary (1958) presented an early version of HF theory and the possibility of fracture control. Since then, many theoretical and experimental investigations have been conducted (i.e. Zoback et al., 1977; Schmitt and Zoback, 1989; Haimson and Cornet, 2003).

The underground formations are subjected to complex stress fields and affected by various geological processes, as described by Amadei and Stephansson (1977) and Zang and Stephansson (2010). The magnitude and direction of the principal stresses are important in HF because they control the amount of pressure required to create and propagate a fracture, the direction of the fracture and the fracture shape. The direction that a fracture induced by HF takes in a rock is also a function of several variables, including anisotropy of rock strength. Sun et al. (2011) investigated fracture extension during HF in oil shale and found that the fractures are elliptical and that fractures extend along different directions due to anisotropic properties and the in situ stress condition.

Ishida et al. (2004; 2012; 2013) have previously conducted HF experiments using carbon dioxide (CO₂), water, and viscous oil and found that low viscosity fluids such as

CO₂ tend to induce widely extending fractures with many branches. These fractures should be better suited for producing shale gas because they have a larger surface area within the shale than those induced by water.

Accordingly, by monitoring acoustic emissions (AE), this study focuses on the fracture growth in shale cores in relation to the effects of stress condition and anisotropy due to sedimentary planes. This chapter also examines the effect of the viscosity of various fracturing fluids (viscous oil, water, and CO₂) on the fracture mode and on the microscopic features of the induced fractures. The results might be beneficial in industrial energy projects such as extraction of unconventional gas from shale and the sequestration of greenhouse gases.

3.2 Methods

3.2.1 Cores and Experimental Setup

Experiments were performed on six cylindrical shale cores measuring roughly 170 mm in length and 85 mm in diameter. All samples were retrieved by drilling blocks obtained from a depth of 275 m below sea level while mining a drift at the *Kushiro* coal mine in *Hokkaido, Japan*. The blocks were sandy shale from Palaeogene *Harutori* coal bearing formation. Because sedimentary planes were clearly observed on the surfaces of the blocks, the drilling direction was selected to be normal to the sedimentary plane.

A hole for hydraulic fracturing with a diameter of 10 mm was drilled in the side of the core at the vertical midpoint. A Cartesian coordinate system was applied to the cores: the *Z* axis was set along the cylindrical axis and normal to the sedimentary plane, the *X* axis was set along the drilled hole, and the *Y* axis was set orthogonal to the other 2 axes, as shown in Figure 3.1.

P wave velocities were measured along the three selected axes for each specimen. The results of the P wave velocity measurements clearly show orthogonal anisotropy due to the sedimentary bedding with the exceptions of those in the cores K-01 and Kc-12 (Table 3.1).

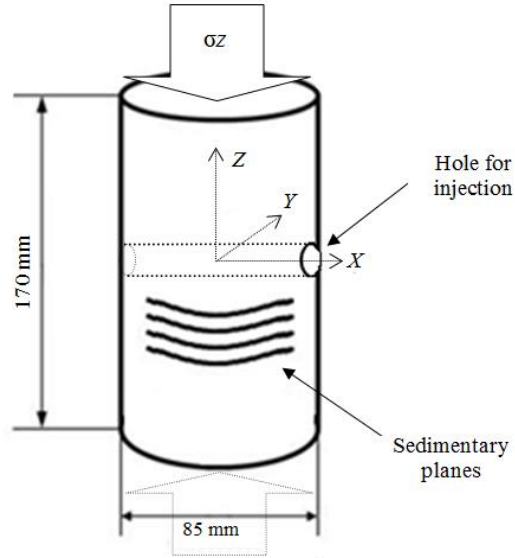


Figure 3.1 Diagram and photograph of the core dimensions and coordinates.

Table 3.1 Anisotropy of P wave velocity along the different axes in shale cores.

Core (No.)	P wave velocity (km/s)		
	X	Y	Z
K-01	3.23	3.11	3.55
K-03	3.12	3.13	2.75
K-04	3.24	3.24	2.92
K-05	3.65	3.36	2.28
K-07	3.00	3.11	2.84
K-09	2.80	3.50	2.87
Kc-01	3.20	3.30	2.90
Kc-06	3.36	3.19	3.10
Kc-07	3.28	3.28	3.01
Kc-12	3.59	3.73	3.82

Hydraulic fracturing tests were run at ambient condition and two uniaxial stresses of 1 and 3 MPa, applied along the Z axis (σ_z , normal to the sedimentary plane). Four strain gauges of 10 mm long were attached to the cores to confirm that loading was uniformly applied to the cores before testing.

3.2.2 Method of Fluid Injection

Three types of fluids, namely, viscous oil, water, and liquid carbon dioxide (L-CO₂), were used for hydraulic fracturing. The viscous oil used was automobile transmission oil (Mahha Super Transmission Oil 75W-90; Fuji Kosan Co. Ltd., Tokyo, Japan). At the experimental temperature, the viscous oil was 270 times more viscous than water, whereas the L-CO₂ has about 1/10 the viscosity of water.

A packer with a pressurizing section of 30 mm was set in the center along the injection hole. Fluids were injected at a constant flow rate of 1 mL/min, and injection pressure was recorded at 0.1 s intervals.

A syringe pump with controllable discharge flow rate was connected to the hole via connector pipes and used to inject the fluid. A pressure transducer was placed at a position close to the packer to detect the actual fluid pressure of the injection.

3.2.3 Methods for Monitoring AE, Pressure, and Temperature

An array of 16 PICO sensors (Physical Acoustics Corporation), which were cylindrical, 3 mm in diameter, and 4 mm in length, with a resonance frequency of around 400 kHz, was used to record AE events.

The detected AE signals were amplified by a total of 84 dB (36 dB in the pre-amplifier and 48 dB in the signal conditioner, except in experiments that used L-CO₂ as fracturing fluid, where signal conditioner was set to 24 dB due to a high level of noise), then recorded on a hard disk via an A/D converter. For each event, the record length and sampling time of the A/D converter were selected to be 2048 words and 0.1 μ s, respectively, with 16-bit resolution. The dead time was set to be 1 ms after recording an event to prevent the hard disk from recording too much noise due to the vibrations following a large AE event. Recording of an AE event was triggered when one of the signals from the 16 sensors exceeded 3 V and the triggered events usually have more than a few signals.

The AE events were monitored and recorded during the injection. Later in the process, the AE hypocenters were located by P wave arrival time at sensors based on a

least squares method and then compared to the results of visual detection in order to trace the shape and orientation of fractures induced on the surface of the cores.

Furthermore, the mode of fracturing was examined by the statistical analysis determining the polarities of P wave initial motion along their respective AE wave forms following Zang et al. (1998) and Graham et al. (2010). Then, depending on their polarity, they were categorized as either compression or dilatation. The number of compressional initial motions and the number of dilatational were counted for each AE event. A ratio of the compressional initial motions to the total number of the compressional and the dilatational initial motions could then be obtained.

3.2.4 Observation of Fractures with Fluorescent Resin

Fluorescence microscopy (Nishiyama and Kusuda, 1994) can be used to visualize fractures and pores in rocks using resin mixed with a fluorescent substance. In this chapter, microscopy was performed on the shale samples fractured by injection of viscous oil and water.

To prepare samples for observation, the cores were soaked in the resin for about a week under vacuum and then heat-treated at up to 90 °C to solidify the resin. Later, cores were cut into sections normal to the fracture plane extension induced by hydraulic fracturing and were prepared for observation on a microscope under ultraviolet light.

3.3 Results

The experiments were conducted on the shale cores by testing each of the three hydraulic fracturing fluids under an ambient condition and two uniaxial stresses of 1 and 3 MPa. The tests were repeated to confirm the tendency of the results, thus yielding a total of 12 tests. Table 3.2 summarizes the test results where the last column shows the orientation of the induced fractures in relation with the stress conditions and the used fracturing fluid.

Table 3.2 Summary of the shale HF experimental results

Core (no.)	Loading stress σ_z (MPa)	Fracturing fluid (viscosity, mPa·s)	Injection rate (ml/min)	Breakdown (MPa)	Detected (Located) AE sources	Fracture orientation
K-01	0.0	Water (1)	1.00	5.24	122 (13)	Parallel to bedding
K-03	0.0	Water (1)	1.00	8.62	72 (32)	Parallel to bedding
K-02	1.0	Water (1)	1.00	13.08	160 (22)	Loading direction
K-04	3.0	Water (1)	1.00	16.44	205 (65)	Loading direction
K-05	0.0	Oil (270)	1.00	9.95	91 (26)	Parallel to bedding
K-07	1.0	Oil (270)	1.00	8.86	244 (62)	Loading direction
K-09	3.0	Oil (270)	1.00	8.86	319 (39)	Loading direction
Kc-01	3.0	L-CO ₂ (0.10)	1.00	6.91	336 (36)	Oblique direction
Kc-06	3.0	L-CO ₂ (0.10)	1.00	6.81	41(00)	Oblique direction
Kc-07	3.0	L-CO ₂ (0.10)	1.00	6.08	169 (42)	Oblique direction
Kc-12	0.0	L-CO ₂ (0.10)	1.00	8.12	245 (55)	Oblique direction

In this section, the results of a typical case for the respective fracturing fluid and loading conditions are shown. The selection of the typical case was made solely on the numbers and quality of the located AE sources to compare the observed surface fractures. The located AE sources are only those that were recorded 1 s before the breakdown to 15 s after the breakdown.

3.3.1 Testing Observations under Ambient Conditions

In the experiments of the cores K-01 and K-03, water was used as the fracturing fluid, without loading (0 MPa stress along the Z axis). Figure 3.2 shows an example of pressure profile in the hydraulic fracturing test of K-03, the pressure built-up and breakdown occurred at 8.62 MPa. In both of the cores, the fracture extended horizontally along a sedimentary plane and was easily traced on the surface of the cores (as in Figure 3.3a).

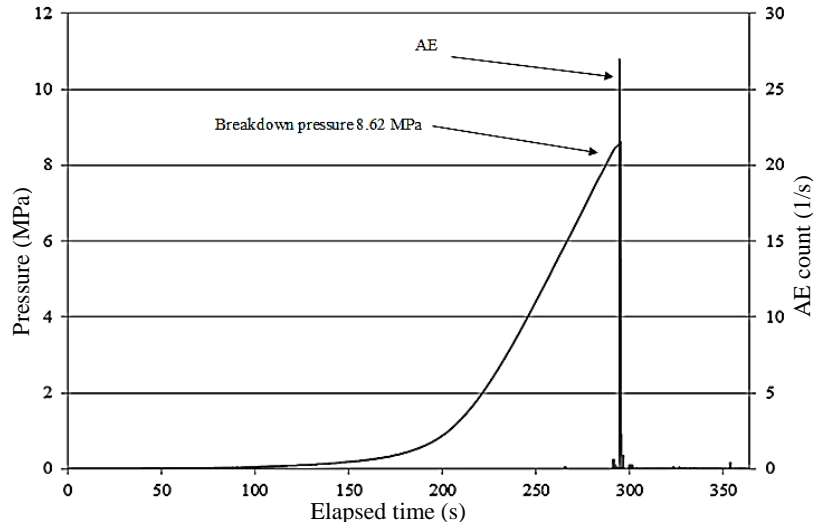


Figure 3.2 Test profile for shale core K-03 (water) under 0 MPa loading.

The AE events detected by the sensors during the fracturing of the cores were located three-dimensionally. Figure 3.3b shows an example of AE sources projections of the core K-03 on the horizontal plane (XY plane) and the two vertical planes (XZ and YZ planes). AE sources seen in the vertical planes are distributed in the horizontal direction. These AE results are consistent with the fracture trace on the surfaces of the cores.

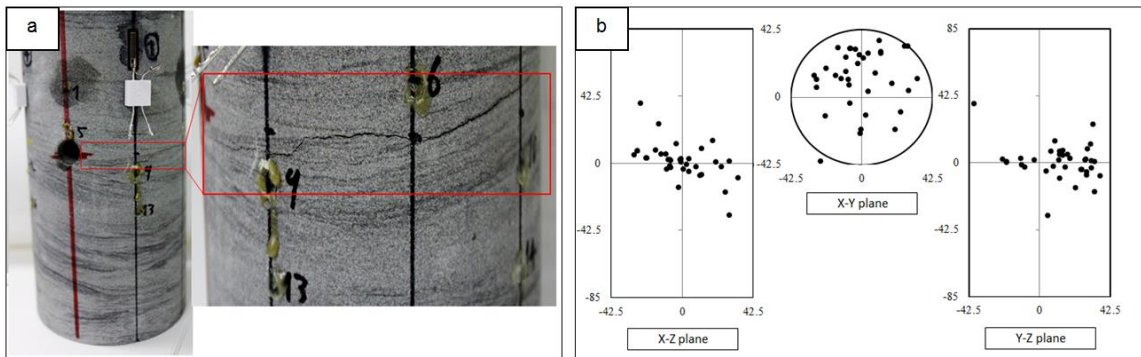


Figure 3.3 (a) Photograph with magnification of observed fracture (red box) on the surface and (b) AE source locations in core K-03 under 0 MPa loading and injection with water.

When a more viscous liquid than water (viscous oil, K-05) was injected, the fracture extended horizontally along the sedimentary bedding, which was the same propagation as that when the fracturing fluid was water. The aperture of the fracture induced was noticeably much larger and clearer (Fig. 3.4a) when the fracturing fluid was oil than when it was water. The projection of the AE source location distribution in YZ plane supports the inference of the fracture path away from its surface trace (Fig. 3.4b).

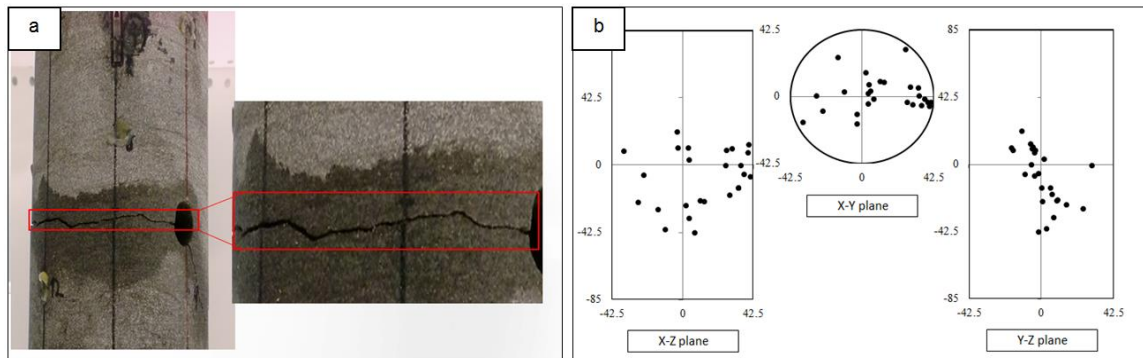


Figure 3.4 (a) Photograph with magnification of observed fracture (red box) on the surface and (b) AE source locations in core K-05 under 0 MPa loading and injection with oil.

The least viscous fluid (L-CO₂) was injected into core Kc-12 under 0 MPa of stress along the Z axis, an intense audible acoustic emission occurred at the moment of breakdown and the fracture extension was not horizontally parallel to the sedimentary planes. This result is unlike the observations recorded for the other fluids, for example the cores K-03 and K-05. Here, the fracture extended in a complex inclined direction and a very large aperture that completely split the core was observed on the surface (Figure 3.5a). Accordingly, the distribution of AE sources locations (Figure 3.5b) showed that the fracture extended at deviated direction of 10° to 30° from the vertical, which is consistent with the clearly traced fracture on the surface.

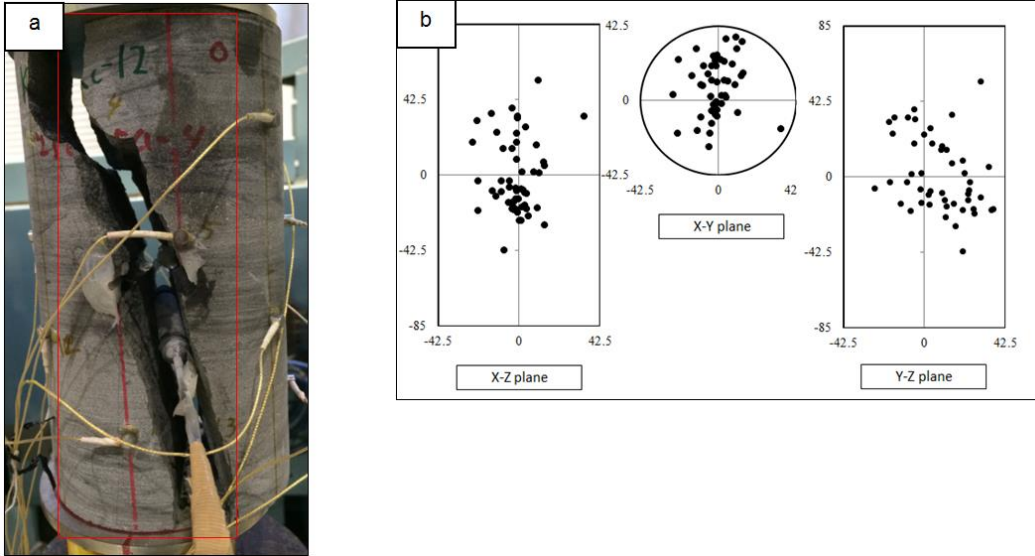


Figure 3.5 (a) Photograph of observed fracture (red box) on the surface and (b) AE source locations in core Kc-12 under 0 MPa loading and injection with L-CO₂.

3.3.2 Testing Observations under Uni-axial loading

In the HF of cores K-02 and K-04 using water as the fracturing fluid, under uniaxial loading of 1 and 3 MPa along the Z axis, the fracture observed on the surface of the cores extended along the loading direction, which was normal to the sedimentary plane. Figure 3.6 shows the case of the core K-04. Both of the cores indicate that the fracture extension was in the loading direction.

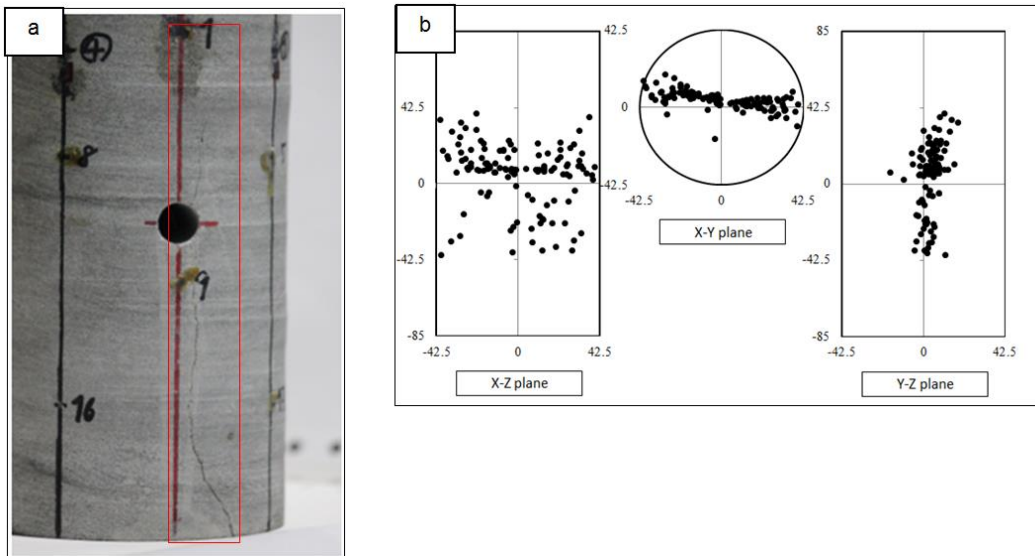


Figure 3.6 (a) Photograph of observed fracture (red box) on the surface and (b) AE source locations in core K-04 under 3 MPa loading and injection with water.

When the other cores (K-07 and K-09) were tested using oil as the fracturing fluid under 1 and 3 MPa of stress along the Z axis, the fracture again extended vertically, normal to the sedimentary plane, the same as when the fracturing fluid was water. Figure 3.7 shows the case of the core K-09. The distribution of the AE sources shows that the fracture extended in the vertical direction (Z axis) in both the XZ and YZ planes, which is consistent with the clearly observed fracture trace on the surface of the cores.

The last experiments were conducted by injecting L-CO₂ in the cores Kc-01, Kc-06 and Kc-07 under 3 MPa of stress along the Z axis. The resulted fracture observed on the surface of the core Kc-01 extended in two horizontal bedding planes with an inclined fracture connecting them though it was under loading. As for the last 2 cores, they extended in a nearly vertical, but slightly inclined direction as shown in Figure 3.8 which is the case of the core Kc-07, unlike in the cores injected with water and oil. The distribution of AE sources locations in YZ plane (as in Figure 3.8b) also shows that the fracture extended at deviated direction from the vertical loading direction.

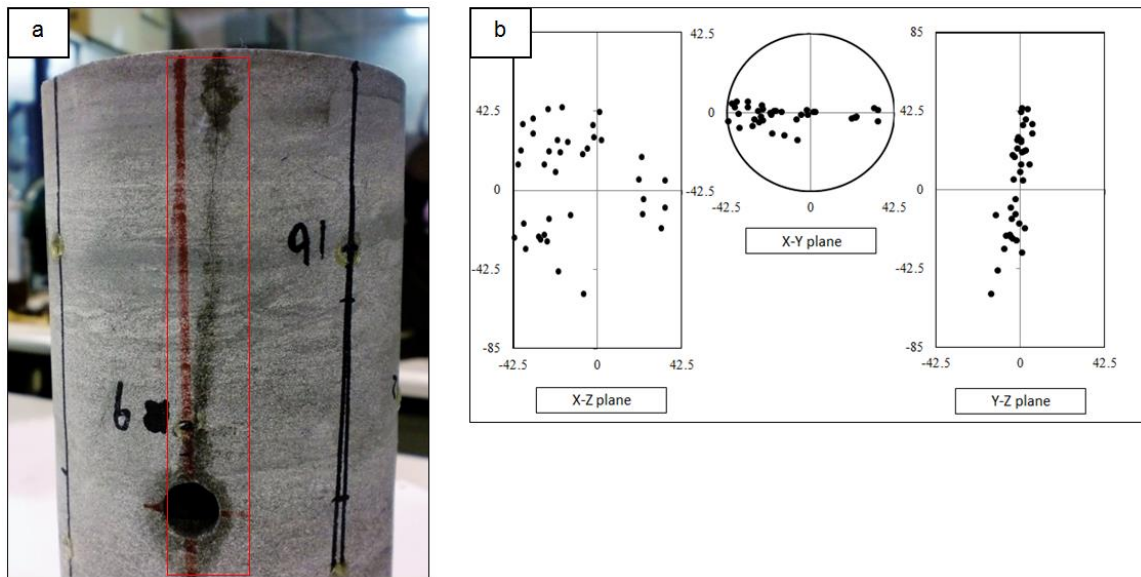


Figure 3.7 (a) Photograph of observed fracture (red box) on the surface and (b) AE source locations in core K-09 under 3 MPa loading and injection with oil.

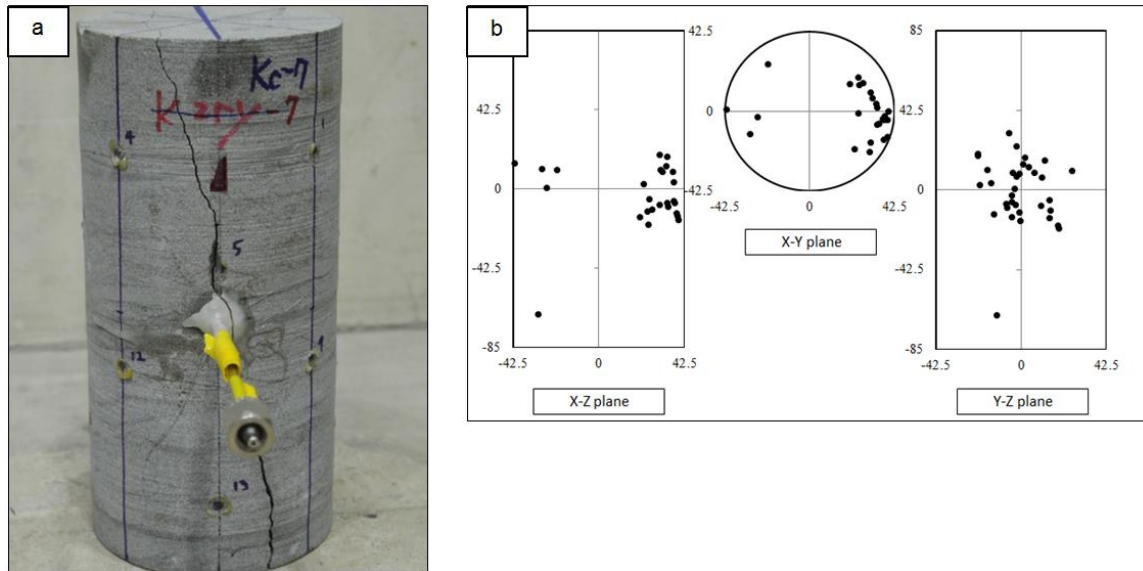


Figure 3.8 (a) Photograph of observed fracture (red box) on the surface and (b) AE source locations in core Kc-07 under 3 MPa loading and injection with L-CO₂.

3.3.3 Analysis of Fracturing Mode

The effect of the difference in fracturing fluid viscosity on the fracturing mode was examined using the cores tested under 3 MPa of uniaxial loading, K-04 (water), K-09 (oil), and Kc-07 (L-CO₂), because the fracture extension under loading seemed to be stable and more clearly affected by fluid viscosity than in the cores without loading, due to the decreasing effect of the sedimentary planes.

To classify the polarities of the P wave initial motion arrivals as either compressional or dilatational, a polarity calibration test was performed by dropping a steel ball on one side of a steel plate after attaching sensors to the other side. A compressional wave resulted from the impact and was recorded at the sensors attached to the opposite side of the plate. Because the upward trace was recorded in all P wave initial motion arrivals in this test, the upward trace was recognized and considered as the compressional motion.

The ratios of the compressional to the total initial motions were obtained for 30 large events each for the viscous oil, water, and L-CO₂ injection. The selection of these events was based on the events causing initial motion on at least 12 out of the 16 motion

sensors. The analysis revealed that higher compressional motion ratios at 60–90% for the viscous oil injection, while 40–60% for the less viscous water and the L-CO₂ injections (Figure 3.9).

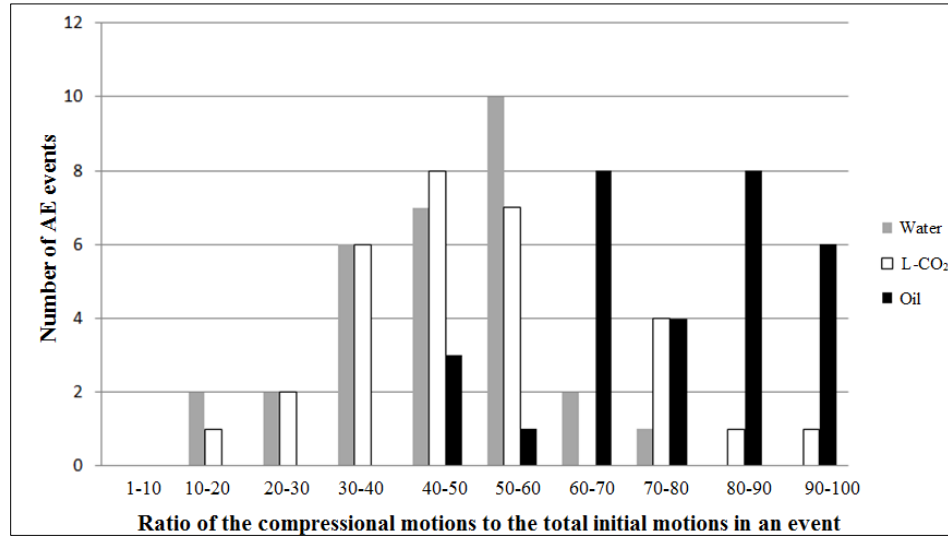


Figure 3.9 Polarity ratios of compressional initial motions in 30 AE events for each hydraulic fracturing experiment using viscous oil, water, and L-CO₂.

The ratio should be 100% for Mode I fracture (tensile fracture) and should be 50% for Mode II fracture (in-plane shear fracture). Thus, these results indicate that the injection of viscous oil tended to induce Mode I fracture, whereas the injection of water and L-CO₂ tended to induce Mode II fracture.

3.3.4 Microscopic examination of fractures

The opening of the fracture in the K-05 sample (oil) is somewhat wider than that in the K-03 sample (water), as can be seen by comparing Figures 3.3a and 3.4a. However, there is no marked difference in the fractures between the two samples under loading at 0 MPa, which is probably due to the fracture extension running along the sedimentary planes.

Comparing the fractures induced under loading at 3 MPa by water and oil, the core K-04, which was fractured by water, contains more inclined fractures having an angle from the loading direction in its path than the core K-09 by oil, (Figure 3.10).

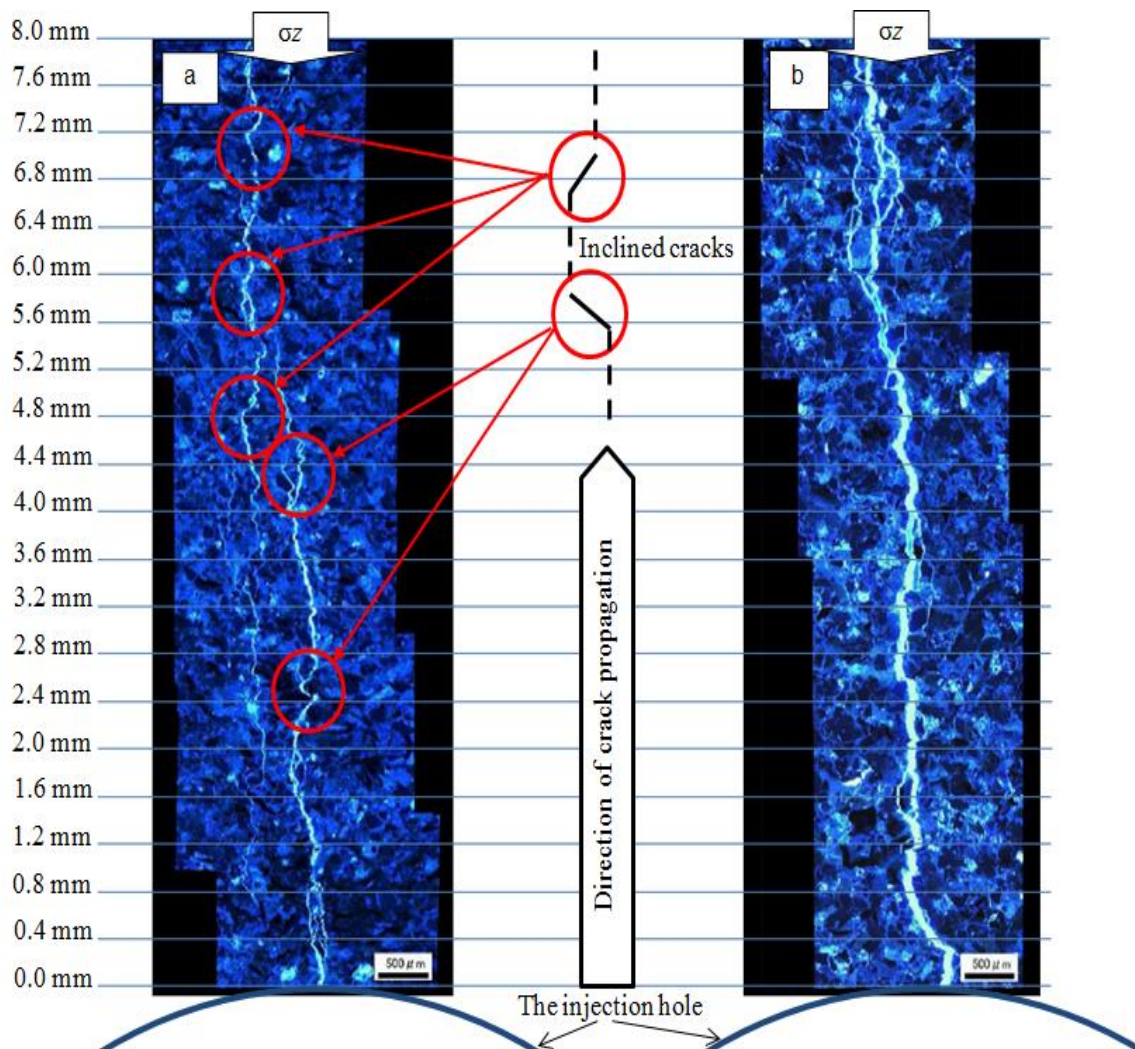


Figure 3.10 Fluorescence microscopy of the fracture shape after (a) injection of water into core K-04 and (b) injection of oil into core K-09. In the both photos, the fractures propagated across the sedimentary planes from the fracturing hole, which is located in the lower end of the photos. The lines of 0.4 mm interval are scanning lines to count numbers of fracture branches shown in Figure 3.11.

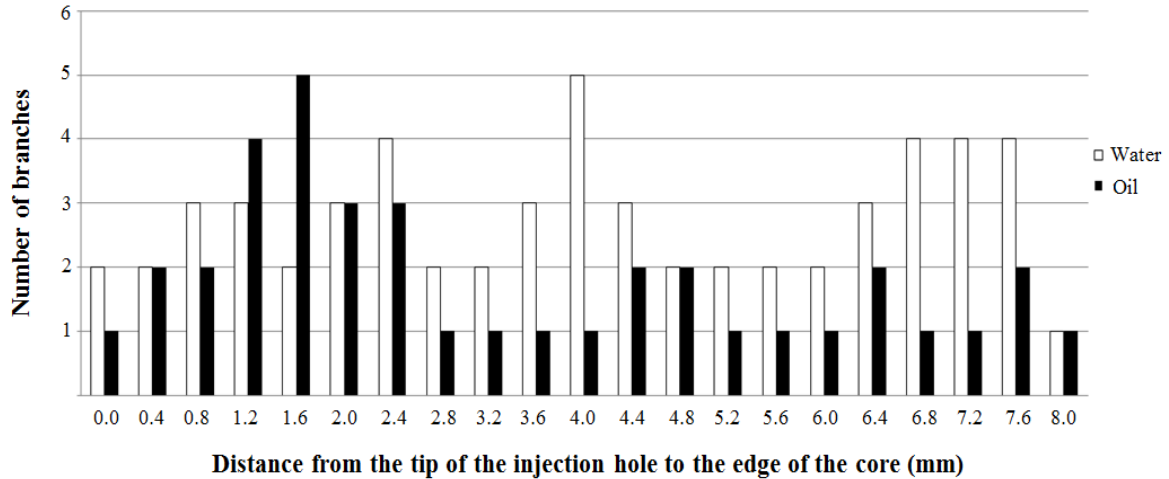


Figure 3.11 Comparing the numbers of fracture branches made by water and viscous oil at the same distance.

On the inclined fracture surfaces, shear stress develops with the angle, and it becomes the maximum at the angle of 45 degrees to the loading axis. Thus, the fracture feature having the inclinations in its path more easily causes shear fracture than that of oil, being consistent with the tendency of fracture mechanism shown in Figure 3.9.

3.4 Discussion

From the results of the experiment, the following tendency regarding fracture extension from the surface fracture and AE source distribution observations was found; In the experiments that used water or oil as the fracturing fluid, fractures tended to extend along the loading direction normal to the sedimentary plane with uniaxial loading and tended to extend along the sedimentary plane if tests were run without loading. The elastic theory indicates that a fracture extends in the direction of maximum compressive stress. Thus, the direction of fracture extension under uniaxial loading in the present study is consistent with elastic theory. When there was no loading, the fracture extended along the weakest plane due to the sedimentary bedding, even though elastic theory indicates that the fracture can extend in any direction.

These experimental results suggest that the direction of fracture extension is strongly affected by in situ stress condition and rock-strength anisotropy. Taking these findings to the field application, if shale strata are horizontally situated and horizontal

stress is large, the fractures induced by hydraulic fracturing will tend to extend horizontally. In contrast, when vertical stress is large relative to horizontal stress, for example in a shale stratum at great depth, the fractures will tend to extend vertically, normal to sedimentary planes, and may extend into a different stratum neighboring the shale.

In the experiments using L-CO₂ as a fracturing fluid, fracture extension shows an independency of loading condition and the presence of bedding plane unlike in those using water and oil. As observed in the results, the fracture extension is different among the cores tested by L-CO₂ even when the same conditions of loading applied. The unstable tendency independent of the loading condition might be due to the specific properties of L-CO₂.

The fracture mode can be identified by examining the polarities of P wave initial motions and obtaining ratios of the compressional initial motions to a total number of initial motions. The ratio should be 100% for Mode I fracture (tensile fracture) and 50% for Mode II fracture (in-plane shear fracture). Thus, the results of these experiments indicate that the viscous oil injection tends to induce Mode I fracture, whereas both water injection and L-CO₂ injection tend to induce Mode II fracture.

In order to quantify the difference caused by different viscosity, a statistical analysis of the number of branches created by water and oil is carried out. The fractured samples were cut and the section of 8 mm in length from the injection hole along the fracture path is observed by setting 20 scanning lines of 0.4 mm interval (Figure 3.10). By counting the number of fractures that cross the scanning lines (Figure 3.11), the injection of oil seems to create branches at only few parts of the fracture path, while the water injection creates random number of branches at any point of the fracture path. Also it is noticeable that the total number of fractures branches resulted by water injection, 55, is larger than those resulted by oil injection, 38, although this observation is restricted only in the section close to the injection hole.

Furthermore, fractures inclining to the loading direction and branching from a main fracture were mainly observed in samples fractured with water. In addition,

because shear stress develops on an inclined plane with an angle from the loading direction, the difference in the fracture feature is consistent with the AE monitoring results that Mode II AE events increased with decrease of the fluid viscosity as shown in Figure 3.9.

The fracture extension in shale HF by L-CO₂ appeared to be unstable even in the same stress condition. This seems to be strongly affected by the difference of fracturing mode due to viscosity of the fracturing fluid, unlike in other fluids, because the viscosity of L-CO₂ is 1/10 and 1/2700 that of water and viscous oil, respectively (see Table 3.2). Since the slick nature of L-CO₂ makes it easily able to fill even the tiniest spaces, fracture extension most likely becomes very sensitive to even small defects in the core. In addition to the low viscosity, the phase of CO₂ changes from liquid to gas corresponding to the pressure decrease after fracture extension. Since the compressibility of the gas is much larger than that of the liquid, expansion of CO₂ gas may help to connect defects inside of a core and cause the fracture to extend in an inclined direction, and also result in a much larger sound than that in water or oil injection at the moment of fracture.

The hydraulic fracturing experiments in granite specimens using supercritical and liquid state carbon dioxide, water, and viscous oil discussed in chapter 2 revealed that low viscosity fluids like CO₂ tend to induce widely extending fractures with many branches and with the dominant fracture type being Mode II. The experimental results for the shale cores in this chapter seem to be consistent with the tendency observed in granite specimens, particularly with the tendency that fracture extension with Mode II dominant fractures during CO₂ injection is very sensitive to defects, such as tiny spaces in a core.

CO₂ fracturing, as opposed to conventional slick water fracturing, can likely induce fractures with better features for shale gas production, for example, a larger surface area. In addition, there is a possibility for CO₂ to be used for enhancing shale gas production and recovery (Kalantari-Dahaghi 2010), because shale's affinity for CO₂ is stronger (about 5 times greater) than the affinity for methane (Nuttall 2006) and displacement of absorbed methane (shale gas) with CO₂ is also expected. Taken together, these findings suggest that CO₂ fracturing is a promising new method for shale gas recovery.

3.5 Conclusions

Based on the dependency on fracturing fluid viscosity of AE distribution, the fracturing mechanism deduced from ratios of the P wave first motion polarity of AE events, and fracture features observed by the fluorescent method, we can draw the following conclusions:

(1) Surface fracture observations and AE source distributions revealed that fractures extended along the loading direction normal to the sedimentary plane under uniaxial loading in the experiments that used water and oil as fracturing fluids. On the other hand, they extended along the sedimentary plane when tests were run without loading. These results suggest that the direction of fracture extension is strongly affected by in situ stress condition. However, the L-CO₂ fracturing did not show this tendency, where fracture extended oblique both to minimum principal stress direction and sedimentary plane which is probably related to its low viscosity.

(2) The ratio of polarity of P wave initial motions indicated that injection of viscous oil tends to induce Mode I fracture and both injection of water and injection of L-CO₂ tend to induce Mode II fracture.

(3) Fluorescence microscopy observation revealed that HF by viscous oil injection produces linear fractures with few branches, whereas hydraulic fracturing by water injection produces fractures with many branches inclining from the loading axis. This is consistent with the differences in fracture mode based on differences in the viscosity of the fracturing fluid, as shown above.

(4) The fracture extension after fracturing with L-CO₂ is unlike those after fracturing with other fluids, which seems to be due to the low viscosity of L-CO₂. This result seems to be consistent with the tendency observed in granite specimens, where low-viscosity fluids like CO₂ tend to induce widely extending fractures having many branches with Mode II fractures being dominant. This pattern of fracturing presents an advantage for shale gas production by fracturing with L-CO₂ over fracturing with conventional slick water.

References

Amadei B. and Stephansson O. (1977). *Rock Stress and its Measurement*. Chapman & Hall.

Arthur J. D., Bohm B. and Layne M. (2008). *Hydraulic Fracturing Considerations for Natural Gas Wells of the Marcellus Shale*. Proceedings of the Ground Water Protection Council Annual Forum, 1-16. Ohio, USA.

Cleary J. (1958). *Hydraulic Fracture Theory Part II - Fracture Orientation and Possibility of Fracture Control*. Division of the Illinois state geological survey, Circular 252.

Graham C., Stanchits S., Main I. and Dresen G. (2010). *Comparison of Polarity and Moment Tensor Inversion Methods for Source Analysis of Acoustic Emission Data*. *International Journal of Rock Mechanics & Mining Science*, 47, p. 161-169.

Haimson B. and Cornet F. (2003). *ISRM Suggested Methods for Rock Stress Estimation—Part 3: Hydraulic Fracturing (HF) and/or Hydraulic Testing of Pre-Existing Fractures (HTPF)*. *International Journal of Rock Mechanics and Mining Sciences*, 40, p.1011-1020.

Hubbert M. and Willis D. (1957). *Mechanics of Hydraulic Fracturing*. *Petroleum transactions AIME*, 210, p.153-168.

Ishida T., Chen Q., Mizuta Y. and Roegiers J. (2004). *Influence of Fluid Viscosity on the Hydraulic Fracturing Mechanism*. *Transactions of the ASME, Journal of Energy Resource Technology*, 126: p.190-200.

Ishida T., Aoyagi K., Niwa T., Chen Y., Murata S., Chen Q. and Nakayama Y. (2012). *Acoustic Emission Monitoring of Hydraulic Fracturing Laboratory Experiment With Supercritical and Liquid CO₂*. *Geophysical Research Letters*, 39, L16309, doi: 10.1029/2012GL052788.

Ishida T., Nagaya Y., Inui S., Aoyagi K., Nara Y., Chen Y., Chen Q. and Nakayama Y. (2013). *AE monitoring of Hydraulic Fracturing Experiments with CO₂ and Water*. *Proceedings of Eurock, Wroclaw, Poland*, p. 957-962.

Kalantari-Dahaghi A. (2010). Numerical Simulation and Modeling of Enhanced Gas recovery and CO₂ Sequestration in Shale Gas reservoirs: A Feasibility Study. Proceedings of International Conference on CO₂ Capture, Storage and Utilization. Society of Petroleum Engineers. New Orleans, Louisiana, USA.

Nishiyama T., and Kusuda H. (1994). Identification of Pore Spaces and Micro Cracks Using Fluorescent Resins. International Journal of Rock Mechanics and Mining Science & Geomechanics Abstracts, 31, p. 369–375.

Nuttall B., Drahovzal J., Eble C. and Bustin R. (2006). CO₂ Sequestration in Gas Shales of Kentucky. Proceedings of the 5th Annual Conference on Carbon Capture and Sequestration, Poster No. 106. Alexandria, Virginia, USA.

Schmitt D. and Zoback M. (1989). Poro-Elastic Effects in the Determination of the Maximum Horizontal Principal Stress in Hydraulic Fracturing Tests; A Proposed Breakdown Equation Employing a Modified Effective Stress Relation for Tensile Failure. International Journal of Rock Mechanics and Mining Sciences & Geomechanics Abstracts, 26, p. 499-506.

Sun K., Tan J. and Wu D. (2011). The Research on Dynamic Rules of Crack Extension During Hydraulic Fracturing for Oil Shale In-Situ Exploitation. Proceedings of International Conference on Environmental Science and Engineering (ICESE 2011). Procedia Environmental Sciences, 12 (2012), p.736-743.

Zang A., Wagner F., Stanchits S., Dresen G., Andresen R. and Haidekker M. (1998). Source Analysis of Acoustic Emissions in Aue Granite Cores under Symmetric and Asymmetric Compressive Loads. Geophysical Journal, 135, Issue 3, p. 1113-1130.

Zang A. and Stephansson O. (2010) Stress Field of the Earth's Crust. ISBN 978-1-4020-8444-7.

Zoback M., Rummel F., Jung R. and Raleigh C. (1977). Laboratory Hydraulic Fracturing Experiments In Intact And Pre-Fractured Rock. International Journal of Rock Mechanics and Mining Science & Geomechanics Abstracts, 14, p. 49-58.

Chapter 4

Stimulated Reservoir Volume in Laboratory Evaluated for the tested samples under Microscopy Using the Fluorescence Method

4.1 Background

The economic viability of producing natural gas from shale formations depends highly on the effective stimulation of reservoirs, which is mainly achieved by combining the horizontal or directional drilling with planned multistage hydraulic fracturing (HF). This practice has been in use for long time and proved successful especially in shale gas reservoirs (Arthur et al., 2008).

The use of low viscosity HF fluids such as CO₂ for well stimulation has been considered because it eliminates formation damage and also reduces the residual fracturing fluid (Sinal and Lancaster, 1987; Liao et al., 2009). In shale gas industry, it is desired to develop new reservoir fracturing and enhanced gas recovery technologies by reducing water usage to guarantee the environmental sustainability and boost individual well production (Peng et al. 2015). Besides, the CO₂ also has higher affinity for shale than the methane (CH₄) does; CO₂ absorption should be preferred to CH₄ absorption with a molecular ratio of up to 5:1 (Nuttall et al., 2006, Nuttall, 2010).

The success or failure of HF often depends on the resulted stimulated reservoir volume (SRV) which is characterized by the quantity and the quality of the induced fractures network (Mayerhofer et al., 2010). To achieve SRV successfully, HF has to create high conductivity fracturing networks as flow paths for gas, in addition it is necessary for HF to activate and connect existing natural fractures to generate large fractures network (Clarkson et al., 2012; 2013).

In all of field applications of HF, the forms of the fracture network is important to the reservoir performance. However, the induced HF networks that represent SRV are difficult to observe in the field. Even in lab experiments, only few attempts to achieve real characterization of the laboratory induced HF network (Kear et al., 2013). In this regard, this study is a trial to investigate the micro-fractures network resulted by

laboratory HF experiments in specimens of shale and granite using three fluids having different viscosity. By using a fluorescent method (Nishiyama and Kusuda, 1994) that can provide the advantage of tracing resulted HF fractures in a thin polished section, and with support of an advanced computerized image analysis that is useful to visualize and evaluate fractures network, the stimulated reservoir volume (SRV) which is characterized by the quantity and the quality of the fractures network can be evaluated.

4.2 Methods

To evaluate difference of resulted SRV due to the difference of fracturing fluid, the specimens subjected to the HF experiments shown in the previous chapters 2 and 3 were used, that is three cylindrical shale cores and three granite cubes having fractures induced by HF using three fluids having different viscosity; oil, water and L-CO₂, omitting the granite cube fractured by SC-CO₂. Thin sections were made and observed under the microscope to compare the influence of different viscosity on the resulting fracturing network.

4.2.1 Rock Samples and HF Experiments

The shale cores were the specimens having fractures induced by the HF experiments in chapter 3. The cores measure 170 mm in length and 85 mm in diameter shown in Figure 3.1 and the experimental conditions were discussed in section 3.2. Table 4.1 shows a summary of the used cores.

Table 4.1 The shale cores used for SRV evaluation and their HF conditions

Core No.	Loading Stress in Z Direction (MPa)	Fracturing Fluid (Viscosity, mPa·s)	Injection Rate (mL/min)
K-09	3.00	Oil (270.00)	1.00
K-04	3.00	Water (1.00)	1.00
K-06	3.00	L-CO ₂ (0.10)	1.00

The granite cubes measuring 170×170×170 mm³ with a 20 mm diameter central hole for fluid injection were used for evaluation of SRV (Figure 2.1). The experimental conditions were discussed in section 2.2. The conditions of HF including viscosities of the fluids used are shown in Table 4.2.

Table 4.2 The over-cored granite cubes used for SRV evaluation and their HF conditions

Specimen No.	Loading Stresses in X, Y and Z Directions (MPa)	Fracturing Fluid (Viscosity, mPa·s)	Injection Rate (mL/min)
G1213	3.00, 6.00 and 4.00	Oil (300.00)	10.00
G1102	3.00, 6.00 and 4.00	Water (1.00)	10.00
G1114	3.00, 6.00 and 4.00	L-CO ₂ (0.10)	10.00

4.2.2 Preparation of Samples for Microscopy Observation

After the HF, the shale cores were soaked in the acrylic resin monomer containing fluorescent compound for one week under vacuum to allow the resin to penetrate into the HF induced fractures, and then heated up to 90 °C in order to solidify the resin, following the fluorescent method proposed by Nishiyama and Kusuda (1994). After that, all of the cores were cut into thin sections with a thickness of 0.03 mm, choosing the cutting direction normal to the fracture extension plane as in Figure 4.1.

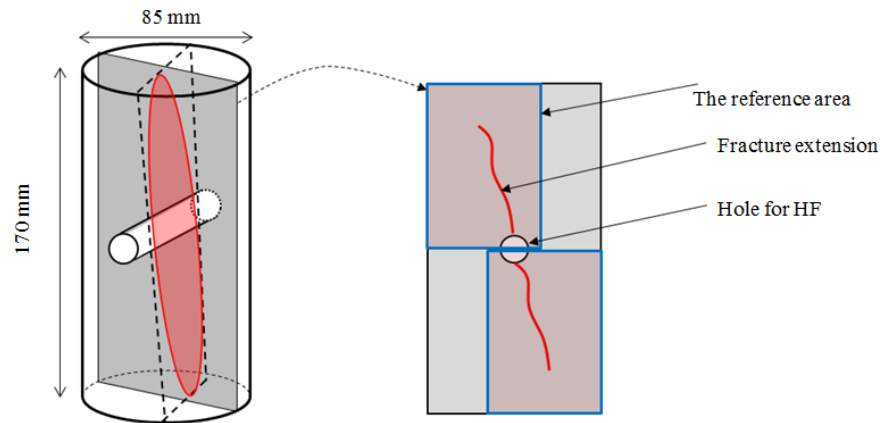


Figure 4.1 Illustrations of the cut plane in shale cores and reference areas on a thin section for microscopic observation.

For the granite, after the HF, over-coring was made along the injection hole using a bit of 68 mm in diameter as shown in Figure 4.2. Then, the cored granite samples were treated with the same manner as the shale cores. For each sample, two thin sections at only one cut plan were made in the two opposite directions from the HF hole along the core's axis, in order to evaluate SRV of fractures induced by HF.

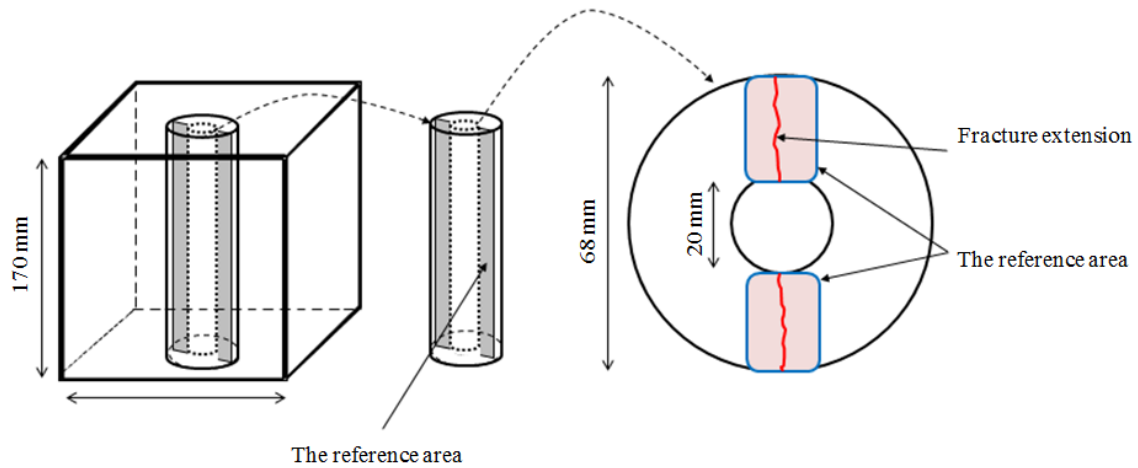


Figure 4.2 The over-cored granite and reference areas for microscopic observation

The cut sections were observed using a microscope at 4 times power magnification under ultraviolet light (UV). The UV reveals fractures and pores where resin exists as brighter parts in contrast to the other normal or un-fractured parts of the rock.

4.2.3 Image Processing and Evaluation Technique

Microscopic images with a resolution of 290 pixels/mm were captured along the fracture paths on the thin polished sections using a digital camera at a shutter speed of 1/15 s. Since the fractures paths in the reference area are too long to be covered in a single image, multiple images were taken. Each of these images covers an area of 17.5 mm × 13.0 mm with resolution of around 19 mega pixels (17.5×290×13.0×290; 19,132,750 pixels/image). The open source software *Image-J* was used to apply image analysis techniques and investigate the area where the resin has penetrated in each image.

Using the microscope under UV, an image of un-fractured shale texture that has no resin traces appears as shown in Figure 4.3a. As the image originally is composed of the red, green and blue components (RGB), it is possible to analyze each component separately. Since the red and the green components are no worthy for the analysis, we applied a threshold of 85 to the maximum intensity of 255 only for blue components of the image. The same image of shale with no resin appears as shown in Figure 4.3b. The

threshold was selected at this level because it is possible to isolate the original shale structure and reveal only the brighter parts if resin has penetrated.

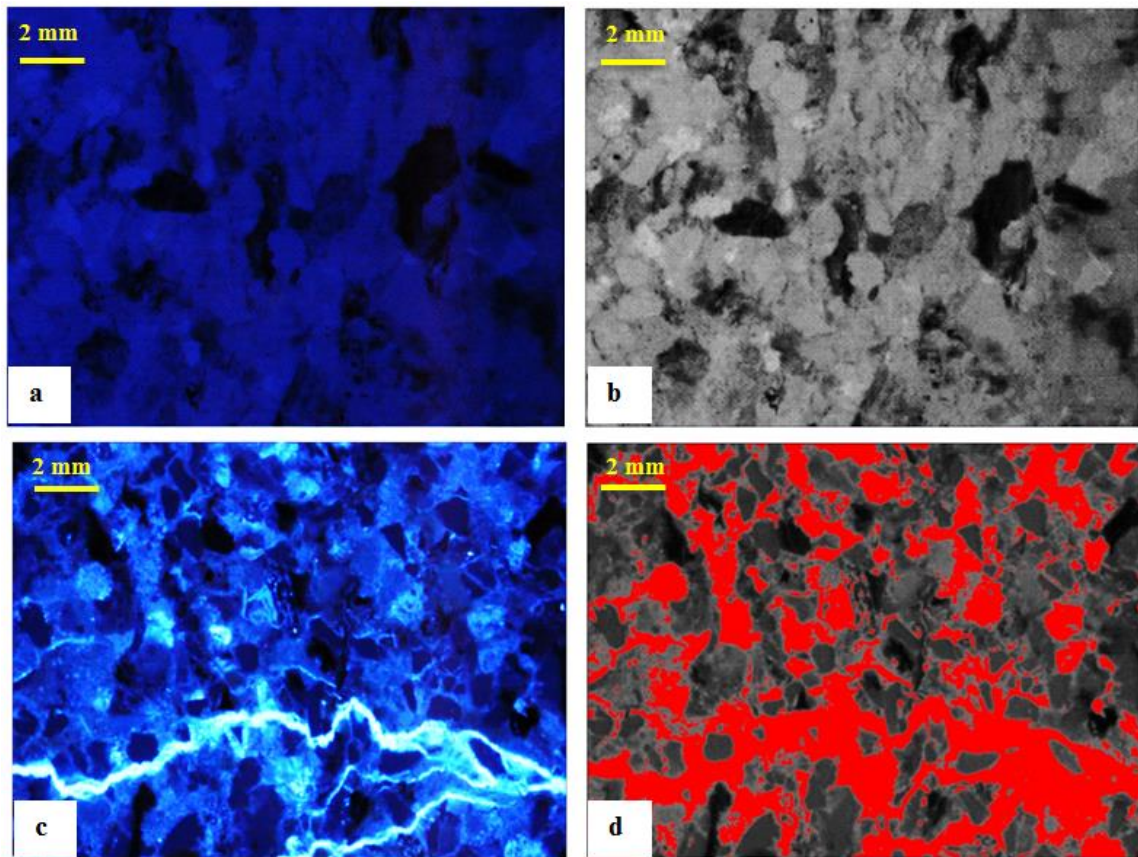


Figure 4.3 Example of images analysis to estimate resin concentration in shale texture; (a) Image on un-fractured shale texture, (b) the same image of un-fractured shale texture after applying thresholding on the blue component of the image (0% of the total number of pixels are highlighted), (c) Image with fracture in the shale texture, and (d) The same image of fractured shale texture after applying thresholding shows resin as highlighted area in red (35% of the total number of pixels are highlighted).

In the other case, if the shale texture contained fractures which are intruded by the resin, the fractures and the nearby area that contains resin appears as shown in Figure 4.3c. The resin reacts to the UV and reflects particularly a bright blue light because of the fluorescence. By applying the same selected threshold of 85 on the blue component only, the image would appear as shown in Figure 4.3d where the parts having intensity of 85 or more are highlighted in a red color.

By defining the highlighted parts as the area where resin has penetrated, we can calculate the percentage of the resin penetrated area for each image composed of 19,132,750 pixels, by counting number of the pixels highlighted. For example, in the image of Figure 4.3d, the number of the pixels highlighted in the red color was 6,696,462 and the number of total pixels of the image was 19,132,750; the percentage was calculated to be 34.9%.

4.3 Results and Discussion

Using the methodology described in the section 4.2.3, the first step is done by selecting images with at least one pixel having intensity higher than 85 among the 19,132,750 pixels. In the case of shale, the counted number of selected images was 561, 408 and 1167 for oil, water and L-CO₂ respectively. This result indicates that an area where the resin reached even if the amount is very small, it is larger by L-CO₂ than those by water and oil.

For the selected image with at least one pixel having intensity higher than 85, in other word, excluding images having no pixel having intensity higher than 85, the number of images was counted for every 10% difference in the percentage of the resin penetrated area for each HF fluid, as shown in Figure 4.4. For example, in HF of shale by L-CO₂, the number was 296, 75 and 88 for images having the resin concentration of less than 0-10%, 10-20% and 20-30% respectively.

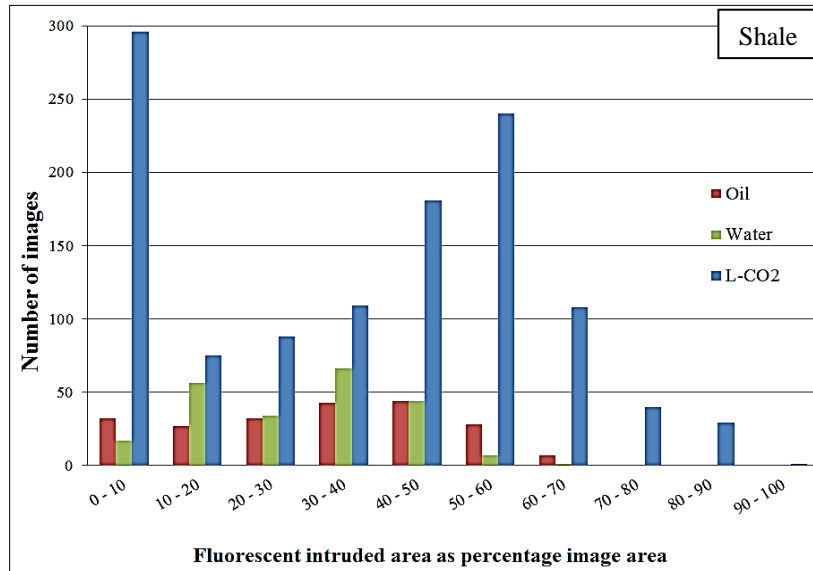


Figure 4.4 Distribution of counted images in shale for every 10% difference in the percentage of the resin penetrated area for each HF fluid.

In the figure, there is no large difference between the cases of oil and water. In comparison to these cases having their peaks at 30-50%, L-CO₂ shows a peak from 50-60% and the distribution extended to reach up to more than 90%. This indicates that L-CO₂ has created fractures in a larger area and the resin reached and penetrated further away from the main fracture, whereas oil and water created fractures only in the vicinity of main fracture and the resin reached only in and around the main fractures. In addition, in the figure, there are a large number of images with low percentage of less than 10% in HF by L-CO₂ compared to the other two fluids. Associated with the fact that the number of images with at least one pixel having intensity higher than the threshold of 85 is much larger in the case of L-CO₂ than those in water and oil, this result also indicates that L-CO₂ created fractures in a larger area, as indicated by the spread of resin.

The same method of analysis was applied to the case of granite HF, the number of the selected images with at least one pixel having intensity higher than the threshold of 85 was 144, 147 and 443 for oil, water for L-CO₂ respectively. The tendency that the number of L-CO₂ is much larger than those of oil and water is quite similar to that of shale.

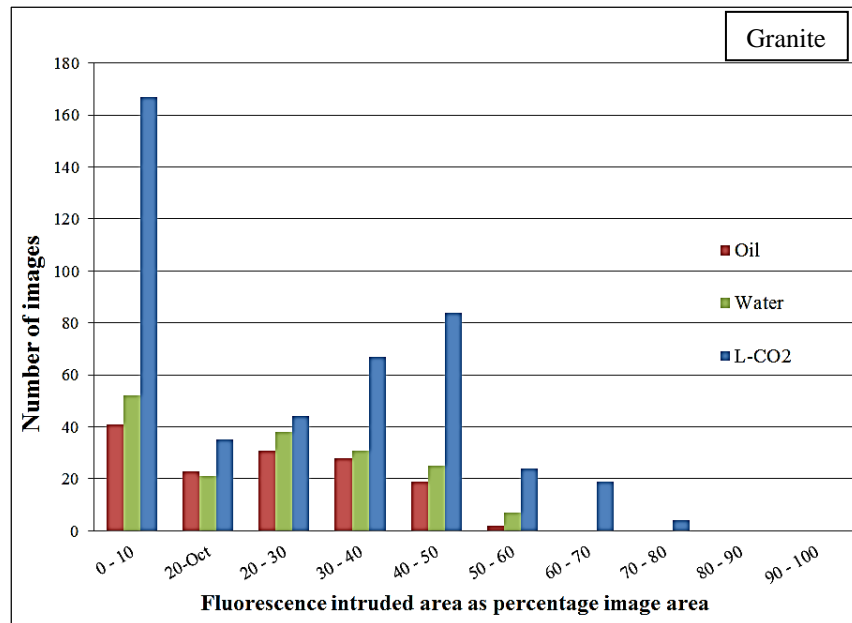


Figure 4.5 Distribution of counted images in granite for every 10% difference in the percentage of the resin penetrated area for each HF fluid.

Figure 4.5 shows the results obtained by the same statistical analysis applied to the shale shown in Figure 4.5. The case of L-CO₂ peaks around 50% and extended to reach up to more than 70%, compared to those of oil and water showing peaks at 20-30%. These results suggest that HF by L-CO₂ created an area larger than those by oil and water, which covered only a narrow area around the main fracture, as well as in the case of HF in the shale cores.

The distinct differences of L-CO₂ in results obtained in both of shale and granite in comparison to the other two HF fluids most likely is due to the low viscosity nature of L-CO₂ because of its ability to fill in the tiniest pore spaces and micro fractures easily. In addition to the low viscosity, CO₂ changes from liquid phase to gas phase corresponding to the pressure decrease due to extension of the new fractures. The expansion of CO₂ in the gas phase may help to connect channels within the rock and also results a much larger network fracturing compared to those resulted by oil or water injection under the same condition. This may explains why the case of L-CO₂ has the widest stimulated area and the highest density of micro-fractures.

As discussed in chapter 2, the source location and mechanism analysis of the monitored AE revealed that low viscosity fluids like CO₂ tend to induce widely extending fractures with many branches and with the dominant fracture type being Mode-II. The fracture observation and acoustic emission monitoring for the shale cores in chapter 3 seem to be consistent with the tendency observed in the granite specimens discussed in chapter 2. As suggested in chapter 3, fracture extension with Mode-II dominant fractures during L-CO₂ injection is very sensitive to tiny defects, such as weak planes or pores in the core.

In another study (Chen et al., 2013), the microscopic observation of using fluorescent method revealed that HF by viscous oil injection produces linear fractures with few branches, whereas HF by water injection produces fractures with many branches inclining from the loading axis. The findings of this study seem to be consistent with the findings by other studies.

As there are many laboratory and field techniques to observe fracture propagation, and every diagnostic technique has its advantages and limitations (Warpinski, 1996). In most cases, fracture observation techniques can provide important data. However, fracture observation techniques have disadvantages which limit its widespread use in industry.

Difficulties in fracture observation methods rely on the fact that fractures are thin compared to their lengths and heights; that is, the methods can essentially detect only two-dimensional anomalies. For example, X-ray computed tomography (CT) has previously been applied to observe fractures propagation in rocks (Johns et al. 1993; Hirono et al., 2003; Jia et al., 2013). The X-ray CT is nondestructive method that can provide 3-D images without damaging of rock samples, however, there is some uncertainty regarding the resolution. The use of micro-CT may overcome this problem (Ketcham and Carlson, 2001; Fukuda et al., 2012; Cnudde and Boone, 2013). Micro-CT is used to visualize and analyze the dynamic processes and thus provide better insights in the rock structure. However, like any other technique, it still has limitations and it may be difficult to observe fractures with apertures less few micrometers.

In comparison, despite the fact that it works only on 2-D, the fluorescence microscopy (Nishiyama and Kusuda, 1994) used in this study is good for obtaining high resolution images for directly determining fracture propagation and variation in aperture.

4.4 Conclusions

Based on the statistical results of SRV and fracture features observed by the fluorescent method, we can draw the following conclusions:

(1) In comparison to the previous SRV studies, the fluorescent method could provide direct information on the difference of SRV induced by different HF fluids.

(2) The observation and statistical analysis of fractures induced in HF by three different fluid viscosities using the fluorescent method showed ability of L-CO₂ injection to achieve effective stimulation. The results suggest that employing a low viscosity fluid in HF of shale reservoirs can achieve more productive network with better SRV.

(3) The observation in this study is highly consistent with the tendency observed in experiments using shale and granite specimens shown in chapter 2 and chapter 3.

References

Arthur J. D., Bohm B. and Layne M. (2008). Hydraulic Fracturing Considerations for Natural Gas Wells of the Marcellus Shale. Proceedings of the Ground Water Protection Council Annual Forum, 1-16. Ohio, USA.

Chen Y., Suzuki T., Kusuda H., Bennour Z., Tomita K., Nagaya Y., Inui S., Nara Y., Ishida T., Sekine K., Nagano Y., Chen Q., and Nakayama Y. (2013). Crack Observation of Cracks Extended by Hydraulic Fracturing in Shale Samples. Proceedings of the Mining and Material Processing Institute of Japan (MMIJ) Spring Meeting, Tokyo, Japan, p. 69-70.

Clarkson C., Nobakht M., Kaviani D. and Ertekin T. (2012). Production Analysis of Tight-gas and Shale-gas Reservoirs Using the Dynamic Slippage Concept. SPE Journal, v. 17/1, p. 230-242. SPE-144317-PA.

Clarkson C., Solano N., Bustin R., Bustin A., Chalmers G., He L., Melnichenko Y., Radlinski A. and Blach T. (2013). Pore Structure Characterization of North American Shale Gas Reservoirs Using USANS/SANS, gas adsorption, and mercury intrusion. Journal of Fuel, v.103, p. 606-613.

Cnudde V. and Boone M. (2013). High-Resolution X-Ray Computed Tomography in Geosciences: A Review of the Current Technology and Applications. Earth-Science Reviews, 123, p. 1–17.

Fukuda D., Nara Y., Kobayashi Y., Maruyama M., Koketsu M., Hayashi D., Ogawa H. and Kaneko K. (2012). Investigation of Self-Sealing In High-Strength and Ultra-Low-Permeability Concrete in Water Using Micro-Focus X-ray CT. Cement and Concrete Research, 42, p. 1494–1500.

Godec M., Koperna G., Petrusak R. and Oudinot A. (2013). Potential for Enhanced Gas Recovery and CO₂ Storage in the Marcellus Shale in the Eastern United States. International Journal of Coal Geology, 118, p.95-104.

Hirono T., Takahashi M. and Nakashima S. (2003). In Situ Visualization of Fluid Flow Image within Deformed Rock by X-ray CT. *Engineering Geology*, 70, p. 37–46.

Jia L., Chen M., Sun L., Sun Z., Zhang W., Zhu Q., Sun Z. and Jin Y. (2013). Experimental Study on Propagation of Hydraulic Fracture in Volcanic Rocks Using Industrial CT Technology. *Petroleum Exploration and Development*, 40(3), P. 405–408.

Jiang L., Nishizawa O., Zhang Y., Park H. and Xue Z. (2016). A Novel High-Pressure Vessel for Simultaneous Observations of Seismic Velocity and In Situ CO₂ Distribution in a Porous Rock Using A Medical X-ray CT Scanner. *Journal of Applied Geophysics*, 135, p. 67–76.

Johns R., Steude J., Castanier L. and Roberts P. (1993). Nondestructive Measurements of Fracture Aperture in Crystalline Rock Cores Using X-ray Computed Tomography. *Journal of Geophysical Research*, 98, p. 1889-1900.

Kear J., White J., Bungler A., Jeffrey R. and Hessami, M. (2013). Three Dimensional Forms of Closely-Spaced Hydraulic Fracture. *Effective and Sustainable Hydraulic Fracturing*, Chapter 34, ISBN 978-953-51-1137-5.

Ketcham R. and Carlson W. (2001). Acquisition, Optimization and Interpretation of X-ray Computed Tomographic Imagery: Applications to the Geosciences. *Computers & Geosciences*, 27, p. 381–400.

Khosrokhavar R., Wolf K. and Bruining H. (2014). Sorption of CH₄ and CO₂ on a Carboniferous Shale from Belgium using a Manometric setup. *International Journal of Coal Geology*, 128/129, p.153-161.

Liao S., Brunner F. and Mattar L. (2009). Impact of Ignoring CO₂ Injection Volumes on Post-Frac PTA. *Proceedings of Canadian International Petroleum Conference*. Calgary, Alberta, Canada.

Liu F., Ellett K., Xiao Y. and Rupp J. (2013). Assessing the Feasibility of CO₂ Storage in the New Albany Shale (Devonian- Mississippian) with Potential Enhanced Gas Recovery

Using Reservoir Simulation. *International Journal of Greenhouse Gas Control*, 17, p.111-126.

Mayerhofer M., Lolon E., Warpinski N., Cipolla C., Walser D. and Rightmire C. (2010). What Is Stimulated Reservoir Volume?. *Society of Petroleum Engineers*, 25 (1): doi:10.2118/119890-PA.

Melzer L. (2012). Carbon Dioxide Enhanced Oil Recovery (CO₂-EOR): Factors Involved in Adding Carbon Capture, Utilization and Storage (CCUS) to Enhanced Oil Recovery. *Proceedings of the Annual CO₂ Flooding Conference*, February, 2012. Midland, Texas, USA.

Middleton R., Carey J., Currier R., Hyman J., Kang Q., Karra S., Jiménez-Martínez J., Porter M. and Viswanathan H. (2015). Shale Gas and Non-Aqueous Fracturing Fluids: Opportunities and Challenges for Supercritical CO₂. *Journal of Applied Energy*, 147, p.500-509.

NETL, (2012). Carbon Sequestration Atlas of the United States and Canada, 4th edition. National Energy Technology Laboratory, U.S. Department of Energy, <<http://www.netl.doe.gov/technologies/carbonseq/refshelf/atlasIV/Atlas-IV-2012.pdf> >.

Nishiyama T., and Kusuda H. (1994). Identification of Pore Spaces and Micro Cracks Using Fluorescent Resins. *International Journal of Rock Mechanics and Mining Science & Geomechanics Abstracts*, 31, p. 369–375.

Nuttall B., Drahovzal J., Eble C. and Bustin R. (2006). CO₂ Sequestration in Gas Shales of Kentucky. *Proceedings of the 5th Annual Conference on Carbon Capture and Sequestration*, Poster No. 106. Alexandria, Virginia, USA.

Nuttall B. (2010). Reassessment of CO₂ Sequestration Capacity and Enhanced Gas Recovery Potential of Middle and Upper Devonian Black Shales in the Appalachian Basin. In: *MRCSP Phase II Topical Report*, Oct. 2005 - Oct. 2010. Kentucky Geological Survey. Lexington, Kentucky, USA.

Peng P., Ling K., He J. and Liu Z. (2015). Shale Gas Reservoir Treatment by a CO₂ Based Technology. Proceedings of 2nd Biennial CO₂ for EOR as CCUS Conference. October 4 - 6, Houston, Texas, USA.

Ross D. and Bustin R. (2009). The Importance of Shale Composition and Pore Structure upon Gas Storage Potential of Shale Gas Reservoirs. *Journal of Marine and Petroleum Geology*, 26, p.916–927.

Sinal M. and Lancaster G. (1987). Liquid CO₂ Fracturing: Advantages and Limitations. *Journal of Canadian petroleum technology*, 26(5), p. 26–30.

Warpinski N. (1996). Hydraulic Fracture Diagnostics. Society of Petroleum Engineers, doi:10.2118/36361-JPT.

Weniger P., Kalkreuth W., Busch A. and Krooss B. (2010). High Pressure Methane and Carbon Dioxide Sorption on Coal and Shale Samples from the Paraná Basin, Brazil. *International Journal of Coal Geology*, 84, p. 190-205.

Yuan W., Pan V., Li X., Yang Y., Zhao C., Connell L., Li S. and He J. (2014). Experimental Study and Modelling of Methane Adsorption and Diffusion in shale. *Journal of Fuel*, 117, p. 509-519.

Chapter 5

Conclusions

In shale gas extraction, the goal of hydraulic fracturing (HF) is utilized to create high conductivity fracturing networks as flow paths for gas, and it is also necessary for HF to activate and connect existing natural fractures to generate large fractures network that can be expressed as stimulated reservoir volume (SRV).

The aim of this research focuses on the effect of HF fluid viscosity on fracturing mechanism and the resulting SRV. In addition, this study focuses on features of fractures resulted in HF experiments and how it can be quantified in the laboratory.

In this study, HF experiments were conducted in cubic specimens of granite under tri-axial stresses, using viscous oil, water, L-CO₂ and SC-CO₂. Also, another set of HF experiments were conducted in cylindrical cores of shale under uni-axial stresses, using three types of fracturing fluid: viscous oil, water, and L-CO₂.

In the experiments, AE was monitored to investigate the effect of the viscosity of various HF fluids on induced fracture features and on fracturing mechanism. In addition, this study investigates the micro-fractures network resulted in the laboratory HF experiments in a thin polished section by using a fluorescent method supported by advanced computerized image analysis, to visualize and evaluate induced fractures network and SRV.

Based on the results of AE source distribution, the fracturing mechanism deduced from ratios of the P wave first motion polarity of AE events, and fracture features observed by the fluorescent method, we can draw the following conclusions:

(1) The breakdown pressure increased with viscosity. Thus, the breakdown pressure with the injection of a low-viscosity fluid, such as SC-CO₂, was expected to be lower than that of water, and much lower than that of viscous fluid such as gel used in field operations.

(2) AE source distributions clarified that the average distance, L_{av} , from a source to the maximum likelihood plane and the fractal dimensions, FD , of the source distributions increased with the decrease in fluid viscosity. This suggests that HF using low-viscosity fluid tends to induce extensive three-dimensional fracturing rather than the two-dimensional fracturing observed for high-viscosity fluid.

(3) Ratios of the P wave first motion polarity suggest that a low-viscosity fracturing fluid tends to induce shear dominant fracture, whereas viscous fluids tend to induce tensile dominant fracture.

(4) The microscopic fracture observations showed that the tortuosity of a main fracture and the average number of fractures increased with the decrease in fluid viscosity. This observation was consistent with the results of AE monitoring.

(6) The SRV observation and statistical analysis of the fractures induced in HF showed ability of CO₂ injection to achieve effective stimulation. These results suggest that employing a low viscosity fluid in HF of shale reservoirs can achieve more productive network with better SRV.

The results of this research suggest that CO₂ fracturing induces three-dimensionally sinuous fractures with many secondary branches that achieve a higher SRV, which seem to be desirable pathways for shale gas recovery, enhanced geothermal systems (EGS) and also other processes such as CO₂ capture and storage (CCS).

Publications Featured in this Study

Chapter 2

Publications Appearing in Peer-Reviewed International Scientific Journals

Ishida T., Chen Y., Bennour Z., Yamashita H., Inui S., Nagaya Y., Naoi M., Chen Q., Nakayama Y. and Nagano Y. (2016) Features of CO₂ Fracturing Deduced from Acoustic Emission and Microscopy in Laboratory Experiments. *Journal of Geophysical Research: Solid Earth*, 121. DOI: 10.1002/2016JB013365.

Chapter 3

Publications Appearing in Peer-Reviewed International Scientific Journals

Bennour Z., Ishida T., Nagaya Y., Chen Y., Nara Y., Chen Q., Sekine K. and Nagano Y. (2015) Crack Extension in Hydraulic Fracturing of Shale Cores Using Viscous Oil, Water, and Liquid Carbon Dioxide. *Rock Mechanics and Rock Engineering*, Volume 48, Issue 4, p. 1463-1473. DOI: 10.1007/s00603-015-0774-2.

Publications Appearing in Refereed International Conference Proceedings

Bennour Z., Ishida T., Nagaya Y., Chen Y., Nara Y., Chen Q., Nakayama Y., Sekine K. and Nagano Y. (2014) Fracture Development and Mechanism in Shale Cores by Viscous Oil, Water and L-CO₂ Injection. *Proceedings of the 48th US Rock Mechanics/Geomechanics Symposium*, June 1st-4th, Minneapolis, Minnesota, USA.

Chapter 4

Publications Appearing in Refereed International Conference Proceedings

Bennour Z., Watanabe S., Chen Y., Ishida T. and Akai T. (2016) Evaluation of Stimulated Reservoir Volume Using the Fluorescence Method in Hydraulic Fracturing of Shale Cores. *International Conference on Geo mechanics, Geo-energy and Geo-resources IC3G*, September 27-29th, Melbourne, Australia.

To be submitted to Peer-Reviewed International Scientific Journal

Bennour Z., Watanabe S., Chen Y., Ishida T. and Akai T.

Evaluation of Stimulated Reservoir Volume in Hydraulic Fracturing Experiments of Shale and Granite Using the Fluorescence Method.